UNIVERSITAT POLITÈCNICA DE CATALUNYA
BARCELONATECH
Escola Tècnica Superior d'Enginyeria
de Telecomunicació de Barcelona

Biochemical model for the amoeboid motion of Dictyostelium discoideum cells

Master Thesis
submitted to the Faculty of the
Escola Tècnica d'Enginyeria de Telecomunicació de Barcelona
Universitat Politècnica de Catalunya
by

Nica Gutu

In partial fulfillment
of the requirements for the master in
Physics **ENGINEERING**

Advisor: Sergio Alonso Muñoz
Barcelona, August 31, 2020

Contents

List of Figures

Listings

List of Tables

Revision history and approval record

Revision	Date	Purpose
0	22/06/2020	Document creation
1	28/08/2020	Document revision

DOCUMENT DISTRIBUTION LIST

Name	e-mail
Nica Gutu	nica.gutu12@gmail.com
Sergio Alonso Muñoz	s.alonso@upc.edu

Written by:		Reviewed and approved by:	
Date	27/08/2020	Date	28/08/2020
Name	Nica Gutu	Name	Sergio Alonso Muñoz
Position	Project Author	Position	Project Supervisor

Abstract

Chemotaxis can be understood as the directed cell migration towards a nonisotropic chemoattractant gradient present in the surrounding environment. This response to external chemical stimuli is employed by eukaryotic cells as a central mechanism lying behind biological processes like development, immune response, and metastasis of tumor cells in multicellular tissues, or sourcing of food and formation of pluricellular structures in unicellular organisms [1, 2]. The focus of the following project stands on the model organism *Dictyostelium discoideum*. A biochemical model that pursue to elucidate the molecular mechanisms responsible for polarization of the cell and the locomotion in *Dictyostelium* cells during chemotaxis is studied. The starting point will be a simplified model of a conservative system based on [3], the latter is compound by two coupled networks describing complex interactions between certain phospholipids localized at cell membrane and enzymes from the cytosol. After reproducing gradually the complete model from [3] searching for excitability properties, it will be discussed the influence of such coupling on the system dynamics. Computational simulations of the spatiotemporal behavior in one and two dimensions were performed, using deterministic and stochastic equations, i.e. the Chemical Langevin equation. The incorporation of a dynamic phase field is employed to characterize the cell shape in two dimensions.

Acknowledgements

I would like to express my gratitude to my supervisor Dr. Sergio Alonso Muñoz for his help and guidance, without whom this project would not be possible. Thanks to whom, I was able to learn and deepen in this field of research.
I am extremely grateful to my mother, who have gave me the support and forces to get where I am now and to be the person who I am. Who taught me to see the things in their truly appearance, to follow my instincts and search the beauty and genuineness in the surrounding world.
I am filled with gratitude for your presence in my life, for the support and the happiness you bring me. Thank you, Uri.
I express my thanks to my friends for all the priceless moments. Thank you, Albert, for encouraging me to find my passion for physics. Thank you, Nora, for helping me to focus again on my studies.

1 Introduction

1.1 Model organism: Dictyostelium discoideum

One example of eukaryotic cells that requires chemotaxis as a way to migrate to substantial spots is the cellular slime mould *Dictyostelium discoideum*. Its widespread use being a model organism may be explained considering the striking and short life cycle that it displays, and the simplicity of its culture on nutrient agar plates. Withal, an important part of *Dictyostelium* proteins are more resembling to human orthologs than those from *Saccharomyces cerevisiae* [4]. As long as nutrients are present in abundance in nearby medium, it exhibits a vegetative behavior living as a single motile amoeboid cell that develop randomly oriented pseudopodia. Since the soil habitat that harbor these cells may not always be a constant supply of bacteria, a morphogenetic process emerges in *Dictyostelium* cells after starvation. Therefore, unicellular amoebae begins to act as aggregation centers and secrete chemoattractant cyclic AMP (cAMP) with the purpose to gather together cells into a slug to prevent the nutritional stress. The *Dictyostelium* cells self-organize spatiotemporally at cellular level in a wavelike form due to the cAMP signaling system [5]. The multicellular mass passes through differentiated stages of a developmental programme until forming a fruiting body with spores. Eventually, these spores will be dispersed to new spots to germinate and give rise to new amoeba single cells which may be able to find new food sources [6]. A new cycle of life has been initiated.
Accordingly, *Dictyostelium discoideum* feeds, communicates and forms a multicellular structure due to chemotaxis. This process exhibits three stages: directional sensing of the chemical species, symmetry breaking which leads to cell polarity and, finally, motility due to the formation of pseudopodia associated to a cytoskeletal remodeling, as can be seen in Fig.1. Thus, chemotaxis involves a signal processing system that interprets temporal and spatial external cues and gives rise to oriented motility [7]. Central to this study will be the complex interactions beneath the signaling pathways that trigger the symmetry breaking in *Dictyostelium* cells.

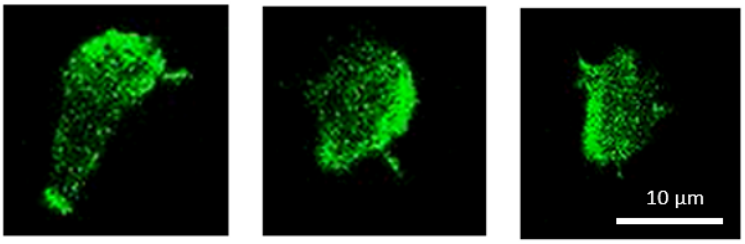

Figure 1: Snapshots of a movie recording *Dictyostelium discoideum*, where the fluorescent part is associated to actin, which links to cell membrane and has affinity to PIP3, leading to the cell movement.

1.2 Cellular symmetry breaking in Dictyostelium discoideum

The network of interconnected signaling pathways leading to cell symmetry breaking and polarity starts with G protein-coupled receptors (GPCR) displaced uniformly along the cell membrane, exclusively in eukaryotic cells. These protein complexes are able to detect external molecules and are responsible for signal transduction pathways. They become activated when certain ligand, e.g. cAMP, binds to them and generates a conformational change, by exchanging

the G-protein bound from GDP to GTP [9, 10, 11, 12]. G-proteins mediate intracellular events as Ras activation, which happens downstream G-protein signaling. Ras is a subfamily of small G-proteins that has a key activity in chemotaxis, among other fundamental cell processes. Due to its binary active (Ras-GTP) and inactive (Ras-GDP) molecular form, it can act as a switch controlling intracellular signaling pathways. Ras is switched on by guanine-nucleotide-exchange factors (GEFs), responsible for catalyzing the reaction from GDP to GTP. The backward reaction is catalyzed by GTPase-activating proteins (GAPs), which inactivates the Ras protein [9]. The cell symmetry is lost when a chemoattractant is approached to a particular side of the membrane, since Ras will be activated only at the edge closest to the gradient [8, 13].
From previous studies, it was found that the chemotactic signaling pathways display properties of an excitable system. Therefore, the interactions between Ras molecules are portrayed in the further work since the asymmetric signals are able to emerge spontaneously due the excitability of this signaling network. The spatiotemporal dynamics of Ras is excitable even in the absence of downstream pathways [3], as I try to prove in the present research. The hallmark of an excitable system is how it responds to an external stimulus depending on whether it is above or not a certain intrinsic threshold. After each excitation we can find a refractory period, in which the system cannot support another excitation. We can determine whether our system is excitable when we find oscillations or traveling waves applying supra-threshold conditions. Two feedback loops are required for such dynamics: one positive-feedback allowing the response to supra-threshold cues in all-or-none manner, and another one negative-feedback which is delayed in order to generate the refractory period [3].
Moreover, Ras-GTP activates phosphoinositide 3-kinase (PI3K), the enzyme responsible for the production of the phoshphatidynolisitol (3,4,5)-triphosphate (PIP3) from phoshphatidynolisitol (4,5)-biphosphate (PIP2), which are phospholipids located on the plasma membrane. This reaction is more catalyzed at the membrane area under a higher cAMP concentration, leading to an accumulation of PIP3, which in turn is responsible for the actin polymerization, that enables pseudopodia formation [14]. While, the reverse reaction is catalyzed by phosphatase and tensin homolog (PTEN): PTEN's substrate is PIP3 and its product is PIP2. This reactions is predominant on the lagging edge of the cell, where the chemoattractant concentration is much lower than in front [15]. The alternation of chemical species between the leading and rear edges induces quick cellular movement: in the front region, polymerized actin induces protrusion activities, whereas at the tail, cell structure is retracted by the contractile force of myosin II [17, 16].
In such a context, we may have two different domains: a PIP3-enriched/PIP2 depleted domain and PIP2-enriched/PIP3-depleted domain. Hence, there are two possible stable states for the same system that can be described as a bistable dynamics, constituting an underlying support for the stationary dynamics of the PIP3-enhanced domain [9]. Building a positive feedback on Ras-GTP from this bistable network can maintain and stabilize the asymmetric signal generation arising from Ras excitability. By coupling these two networks, we can reconstitute the cellular symmetry breaking phenomena present in processes as polarization, migration and division [3]. However, the present study tries to prove that the critical role is played by Ras excitability network.
Establishing a biochemical model for the spatiotemporal dynamics of Ras and PIP3 wave patterns is the main purpose of the current project. The model is constituted by reaction-diffusion equations of two coupled signaling systems: Ras and PIP3, inspired by a previous research [3], presented in Fig.2.

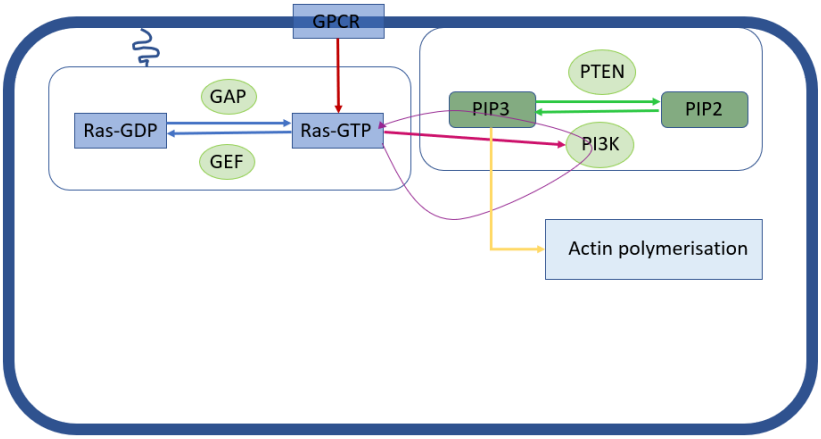

Figure 2: Simplified scheme of a cell highlighting the coupled Ras-PIP3 system at the plasma membrane and illustrating the most relevant reactions for this project at the leading edge during chemotaxis.

The study will start with a simplified conserved model, and step by step, I will include new terms to achieve a complete model capable of reproducing the oscillatory and wave travelling characteristics of an excitable system. Performing analysis of phase space and phase diagrams, I attempt to study the system dynamics and the regime that is interesting for the symmetry breaking. Another focus is settled on the influence of PIP3 positive feedback on Ras spatiotemporal dynamics, which will be considered as almost redundant for Ras wave generation, because chemotaxis is performed even in absence of PIP3 gradient [18]. However, PIP3 needs the activation from Ras to generate waves.
Therefore, a model with the minimal requirements describing such properties considering nonlinear reaction diffusion equations is studied and built from now on. The corresponding simulations to this model are carried out in one dimension and extended to two dimensions. Initially, deterministic equations were considered for the computational study and, finally, stochastic equations, as the chemical Langevin equation. The last part of the project is about reproducing the cell shape using a dynamic phase field. The phase field takes two opposite values depending whether it is inside or outside the cell domain and helps to maintain the no-flux boundary conditions during the cell movement.

2 Background models and recent research

Foregoing efforts were put on the development of a model for the spatiotemporal dynamics of the above mentioned molecular mechanisms to recover the excitable dynamics observed in the chemotactic signaling pathways in *Dictyostelium discoideum* or other similar amoeboid eukaryotic cells. The most relevant articles concerning the model studied in the present work are found in [3, 15]. The theoretical model built in article [15] for the phosphatidynlinositol lipid reactions on the membrane represents the template used in [3] for the dynamics of the Ras signaling system. During the progress of the present work, we can find an analysis of the combined model of the Ras and PIP3 networks from [3].

As a brief summary of the coupled model by Fukushima et al.: first, they considered a conservative model for the PIP3 signaling system, where PIP2 phosphorylation to PIP3 is catalyzed by PI3K and the dephosphorylation from PIP3 to PIP2, by PTEN. These reactions are contemplated as Michaelis-Menten reactions using the maximum reaction rate and Michaelis constant. The activation of PI3K by Ras-GTP is also considered to give account of the PI3K membrane translocation and to trigger other travelling waves. Another MM-type binding reaction diffusion equation is added to describe PTEN interaction with plasma membrane.

To obtain an excitable network for the Ras signaling regulatory system, they applied the model described in [15] as a prototype, where GEFs and GAPs control positive and negatively Ras behavior implementing MM-type enzymatic reactions. The GEFs term involves two elements described as the basal activity of Ras and a positive feedback from PIP3, where arises the coupling between these two networks. The recruitment of GAPs to the plasma membrane is described by two positive feedback mechanisms with a MM-type enzymatic reaction equation. More elements are added to this theoretical model, which will be explained with more details in the further project.

Other mathematical models using reaction-diffusion equations have been suggested to describe the underlying phenomena behind the cell migration in *Dictyostelium discoideum* [19, 20, 21, 22, 26, 27, 28]. Moreover, an auxiliary dynamic phase field is implemented to simulate the cell shape and evolution during the movement. Such a technique for the cell morphodynamics can reproduce deformable boundaries and maintain the no-flux boundary conditions at the edge, and it has already been employed in several studies [20, 23, 24, 25].

3 Project purpose and development

The current work attempts to bring a connection between previous studies related to *Dictyostelium discoideum* spatiotemporal dynamics, illustrating more general mathematical models [20, 24, 25], and a more detailed biochemical model. To have a more biochemical context would allow us to design more appropriate experiments controlling with inhibitor drugs the desired genes expressions. Articles [20] and [24] implement a bistable model with minimum requirements to describe a reaction-diffusion process controlled by an effective concentration giving account for the interplay between activated Ras, PI3K or PIP3. The model presented in [25] consists of a generic wave-forming reaction-diffusion system capable of reproducing bistable and excitable dynamics. The biochemical model studied in [3] is examined to determine whether it is appropriate candidate for the desired role.
The starting point will be a simple conserved model derived of [3] analogous to the classical phosphorylation-dephosphorylation conserved system, which displays monostability. Consequently, new feedbacks will be added to construct bistability. The conservation will be interrupted by including new elements to the system and other enzyme dynamics, obtaining excitability. The complete model will be achieved by studying step by step each case designing algorithms in Python and Matlab to perform phase space and phase diagrams analysis. The reaction-diffusion models are numerically integrated employing finite differences method in one and two dimensions. Finally, to figure out if such a model is capable of cell locomotion, a dynamic phase field is coupled to the system.

4 Results and Discussion

4.1 Simple conserved model, slaving GAPs dynamics

The model studied afterwards and presented in [3] for the Ras excitable network, considering the activation and inactivation from GEFs and GAPs, has the following reaction diffusion equations:

$$\frac{\partial[Ras-GDP]}{\partial t} = R_{GAP} - R_{GEF} + k - \lambda_{Ras-GDP}[Ras-GDP] + D\nabla^2[Ras-GDP] \tag{1}$$

$$\frac{\partial[Ras-GTP]}{\partial t} = R_{GEF} - R_{GAP} - \lambda_{Ras-GTP}[Ras-GTP] + D\nabla^2[Ras-GTP] \tag{2}$$

in which, k stands for membrane association rate of Ras-GDP and $\lambda_{Ras-GDP}$ is the dissociation rate. In Eq. (2), $\lambda_{Ras-GDP}$ is the membrane dissociation rate of Ras-GTP. As we see, R_{GEF} positively regulates Ras by activation, giving Ras-GTP and R_{GAP} inactivates it, producing Ras-GDP. The corresponding equations to the latter terms are:

$$R_{GEF} = \left(V_{GEFs} + \frac{V_{feedback}[PIP3]}{K_{PIP3}+[PIP3]}\right)\left(\frac{[Ras-GDP]}{K_{GEFs}+[Ras-GDP]}\right) \tag{3}$$

$$R_{GAP} = V_{GAPs}[GAPs]\left(\frac{[Ras-GTP]}{K_{GAPs}+[Ras-GTP]}\right) \tag{4}$$

Equations (3) and (4) are characterized as a Michaelis Menten type enzymatic reaction. The first one has two elements corresponding to Ras activation (with the maximum reaction rate V_{GEFs} and Michaelis constant K_{GEFs}) and to positive feedback from PIP3 ($V_{feedback}$ and K_{PIP3}). Equation (4) describes the negative regulation of Ras. The GAPs distribution on plasma membrane is controlled by a positive and negative influence of Ras-GDP and Ras-GTP, respectively, resulting in two positive feedback loops.

$$\frac{\partial[GAPs]}{\partial t} = V_{GAPs_{ass}}[GAPs]_{cyt}\left(\frac{[Ras-GDP]}{K_{Ras-GDP}+[Ras-GDP]}\right)\left(\frac{K_\alpha+\alpha[Ras-GTP]}{K_\alpha+[Ras-GTP]}\right)$$

$$-\lambda_{GAPs}[GAPs] + D\nabla^2[GAPs] \tag{5}$$

$$[GAPs]_{cyt} = [GAPs]_{total} - \chi\overline{[GAPs]} \tag{6}$$

where, in Eq. (5) the MM-type enzymatic reaction (with maximum reaction rate $V_{GAPs_{ass}}$ and Michaelis constant $K_{Ras-GDP}$) stands for the positive regulation from Ras-GDP. Since Ras-GTP has a negative effect on GAPs, the reaction is described with the parameters k_α and α, which are the half-maximum concentration of Ras-GTP for negative regulation of GAPs and the indicator of the negative regulation magnitude of GAPs. In addition, we have Eq. (6) for the GAPs conservation: $[GAPs]_{cyt}$ is the cytosolic concentration, $[GAPs]_{total}$ is the total amount of GAPs available for the reaction, the overline stands for average concentration and χ is a transforming factor from membrane surface concentration to a volume cytosolic concentration. For notation simplicity, Ras-GTP will be designated as X, Ras-GDP as Y and GAPs as Z. As a first assumption, we can slave GAPs dynamics, neglecting the diffusion and considering fast

dynamics:

$$0 = V_{GAPs_{ass}}[GAPs]_{cyt}\left(\frac{[X]}{K_X+[X]}\right)\left(\frac{K_\alpha+\alpha[Y]}{K_\alpha+[Y]}\right)-\lambda_Z[Z]$$
$$Z = \frac{V_{GAPs_{ass}}[GAPs]_{cyt}}{\lambda_Z}\left(\frac{[X]}{K_X+[X]}\right)\left(\frac{K_\alpha+\alpha[Y]}{K_\alpha+[Y]}\right)$$

Substituting this expression in Eqs. (1-2) and choosing $V_{feedback}=0$, we end up with the following model:

$$\frac{\partial[X]}{\partial t} = V^*_{GAPs}\left(\frac{[X]}{K_X+[X]}\right)\left(\frac{K_\alpha+\alpha[Y]}{K_\alpha+[Y]}\right)\left(\frac{[Y]}{K_{GAPs}+Y}\right)-V_{GEFs}\left(\frac{[X]}{K_{GEFs}+[X]}\right)+k-\lambda_X[X]+D\nabla^2[X] \tag{7}$$

$$\frac{\partial[Y]}{\partial t} = V_{GEFs}\left(\frac{[X]}{K_{GEFs}+[X]}\right)-V^*_{GAPs}\left(\frac{[X]}{K_X+[X]}\right)\left(\frac{K_\alpha+\alpha[Y]}{K_\alpha+[Y]}\right)\left(\frac{[Y]}{K_{GAPs}+Y}\right)-\lambda_Y[Y]+D\nabla^2[Y] \tag{8}$$

where, we defined $V^*_{GAPs} \equiv V_{GAPs}\frac{V_{GAPs_{ass}}[GAPs]_{cyt}}{\lambda_Z}$. The similarity with a conserved system of phosphorylation and dephosphorylation processes is remarkable if we forget the membrane association and dissociation rates ($k=\lambda_X=\lambda_Y=0$) and diffusion coefficient ($D=0$) and consider $k_X=0$, $\alpha=1$, for the moment. Thus, the most simple model obtained is:

$$\frac{\partial[X]}{\partial t} = V^*_{GAPs}\left(\frac{[Y]}{K_{GAPs}+Y}\right)-V_{GEFs}\left(\frac{[X]}{K_{GEFs}+[X]}\right) \tag{9}$$

$$\frac{\partial[Y]}{\partial t} = V_{GEFs}\left(\frac{[X]}{K_{GEFs}+[X]}\right)-V^*_{GAPs}\left(\frac{[Y]}{K_{GAPs}+Y}\right) \tag{10}$$

where, $[X]+[Y]=total$, which is considered to be constant. The corresponding scheme to simple system of Eqs.(9-10) is Fig. 3:

Figure 3: The scheme of the model for the simple conserved model without feedbacks ($\alpha=1$, $k_X=0$ $molecules\cdot\mu m^{-2}$).

Plotting the stationary points as a function of the maximum reaction rate V^*_{GAPs}, we can find what type of dynamics displays this system. The system reaches a single stable solution for different values of V^*_{GAPs}, so it is monostable. The maximum stable state that can be found is the total concentration. Therefore, it is interesting to see the system behavior when changing V^*_{GAPs} and the total concentration, represented in Fig.4. For the following analysis, I used $V_{GEFs}=400$ s^{-1}, $K_{GEFs}=3500\ molecules\cdot\mu m^{-2}$ and $K_{GAPs}=40\ molecules\cdot\mu m^{-2}$, listed in the appendices (Tables1-3).

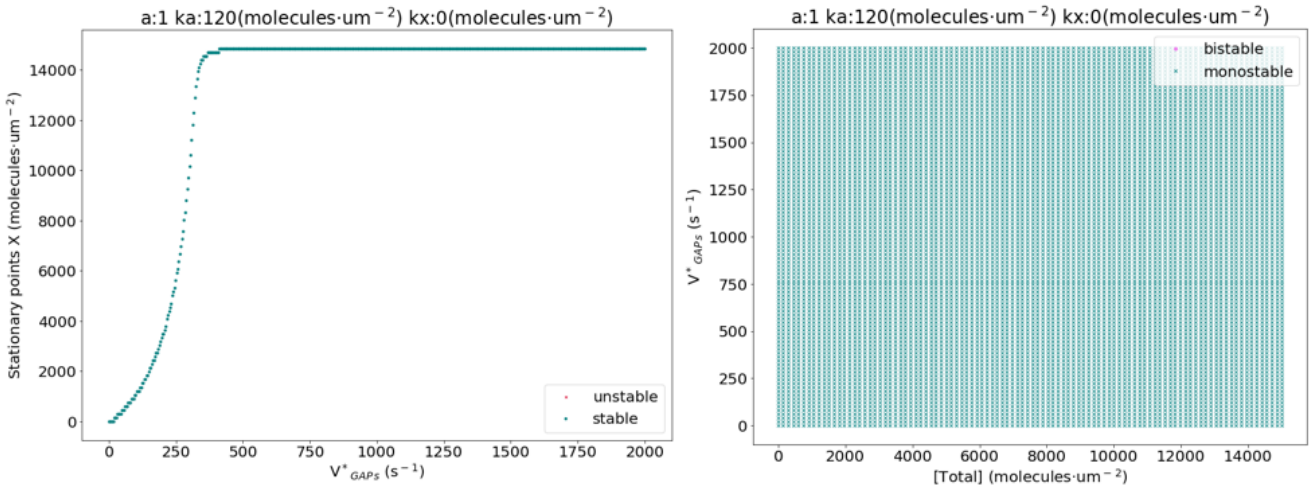

Figure 4: Figure of the stationary points changing V^*_{GAPs} (left) and the phase diagram (right) of the simple conserved model for $\alpha = 1$, $k_X = 0\ molecules \cdot \mu m^{-2}$

GEFs and GAPs have an opposite effect on Ras proteins, same as kinases and phospatases for phosphoproteins. In many cell-signalling networks can be found that these opposite interactions constitute a universal motif. Signalling pathways interpret and transmit external cues from cell membrane to intracellular components using cascades of these motifs. Such cycles may present complex dynamics as bistability or oscillations [29]. Bistability can be obtained introducing a positive feedback in our simple conserved model by setting $\alpha = 0.001$, which corresponds to the positive feedback from Ras-GTP.

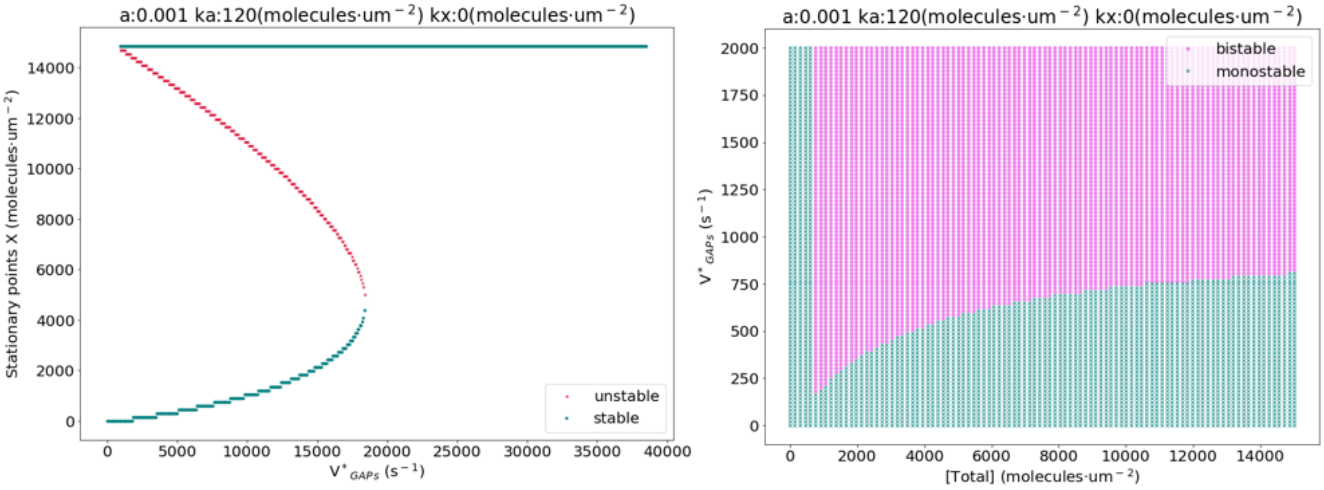

Figure 5: Figure of the stationary points for different values of V^*_{GAPs} (left) and phase diagram for V^*_{GAPs} and total concentration (right) for $\alpha = 0.001$, $k_X = 0\ molecules \cdot \mu m^{-2}$

In Fig. 5 left plot, for a certain region of V^*_{GAPs} value, we obtain three different solutions for the steady-state. There are two stable solutions coinciding with low and high X concentration

and an unstable intermediate state, connecting the other two solutions. When the parameter is increased the system reaches a different stable state unlike for low values, as in a hysteresis. The phase diagram for the parameters V^*_{GAPs} and the total concentration, presented in Fig. 5 right plot, shows us whenever we have one or more steady-state solutions.
The hysteresis shape can be changed by adding the positive feedback from Ras-GDP, $k_X = 3000\ molecules \cdot \mu m^{-2}$. The interactions between the two opposite enzymes result in a bistable switch, as is displayed in the following figure where the high and low concentration can be considered as on and off state:

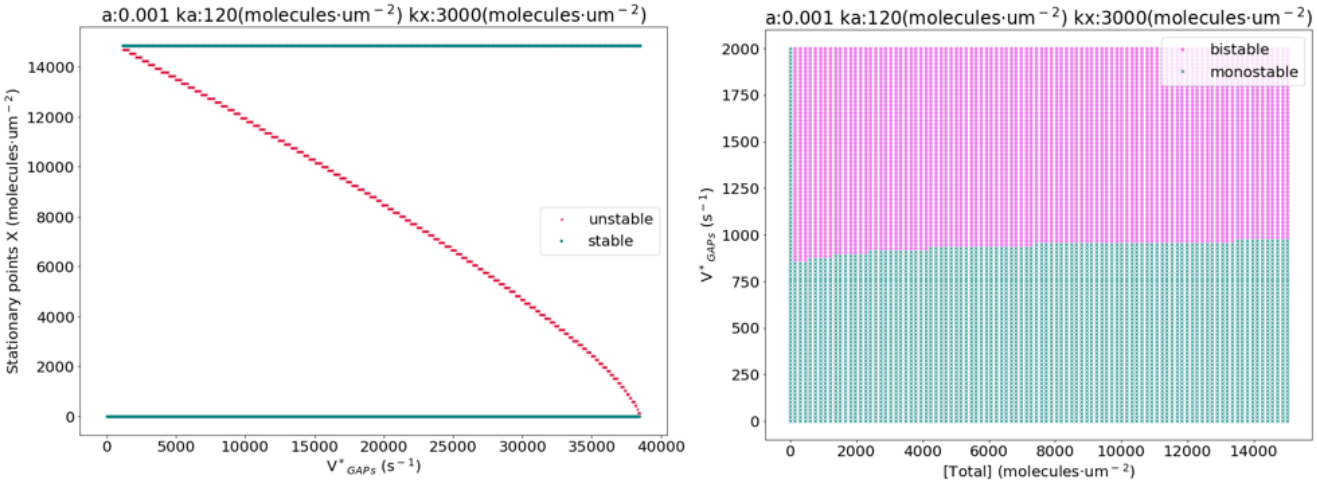

Figure 6: Figure of the stationary points as a function of V^*_{GAPs} (left) and the phase diagram for V^*_{GAPs} controlling the total concentration (right) for $\alpha = 0.001$, $k_X = 3000\ molecules \cdot \mu m^{-2}$

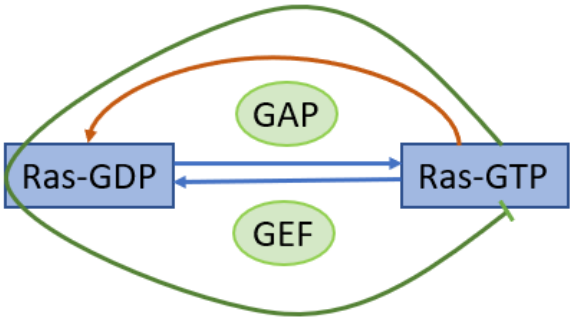

Figure 7: Scheme of the model with the feedbacks from Ras-GTP and Ras-GDP ($\alpha = 0.001$, $k_X = 3000\ molecules \cdot \mu m^{-2}$)

Therefore, a conserved system with two feedbacks (one positive and one negative) affecting the system dynamics, described in Fig. 7, results in a bistable dynamics for a large interval of the parameter V^*_{GAPs}, when it is larger than 800 s^{-1}. As can be seen in Fig. 6, the stable solutions are the low and high concentration, which correspond to zero or total protein concentration. And below $V^*_{GAPs} = 800\ s^{-1}$, the system reaches a single steady-state, regardless the total concentration.

4.2 Model with membrane association and dissociation rates

The conservation is lost whether considering the membrane association and dissociation rate for Ras-GDP (k and $\lambda_{Ras-GDP} \equiv \lambda_X$) and membrane dissociation for Ras-GDP ($\lambda_{Ras-GTP} \equiv \lambda_Y$):

$$\frac{\partial [X]}{\partial t} = V^*_{GAPs}\left(\frac{[X]}{K_X+[X]}\right)\left(\frac{K_\alpha+\alpha[Y]}{K_\alpha+[Y]}\right)\left(\frac{[Y]}{K_{GAPs}+Y}\right) - V_{GEFs}\left(\frac{[X]}{K_{GEFs}+[X]}\right) + k - \lambda_X[X] \tag{11}$$

$$\frac{\partial [Y]}{\partial t} = V_{GEFs}\left(\frac{[X]}{K_{GEFs}+[X]}\right) - V^*_{GAPs}\left(\frac{[X]}{K_X+[X]}\right)\left(\frac{K_\alpha+\alpha[Y]}{K_\alpha+[Y]}\right)\left(\frac{[Y]}{K_{GAPs}+Y}\right) - \lambda_Y[Y] \tag{12}$$

The scheme characterizing the interactions corresponding to the system from Eqs. (11-12) is displayed in Fig. 8.

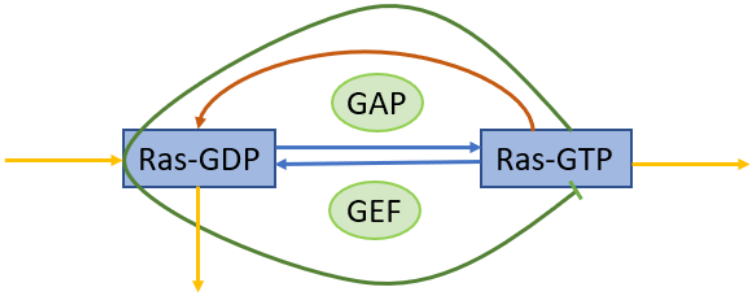

Figure 8: The no-conserved model scheme with $k = 45\ molecules \cdot \mu m^{-2} s^{-1}$, $\lambda_X = 0.003\ s^{-1}$ and $\lambda_Y = 0.2\ s^{-1}$.

The Fig. 9 corresponding to the steady-state solutions of this system as a function of the parameter V^*_{GAPs} allows us to evaluate the displayed dynamics. The parameters K_X, K_α, α, K_{GAPs}, V_{GEFs} and K_{GEFs} have the same values as in the previous section, the entire list can be found in the appendices (Table 2).

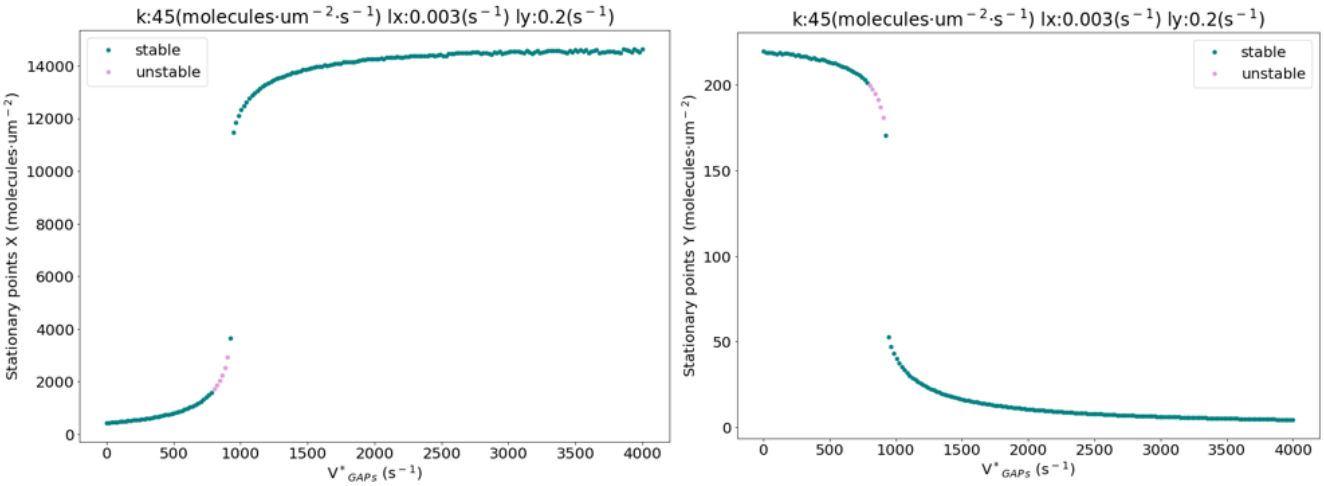

Figure 9: Stationary points of X (left) and of Y (right) controlling V^*_{GAPs} and $k = 45\ molecules \cdot \mu m^{-2} s^{-1}$, $\lambda_X = 0.003\ s^{-1}$ and $\lambda_Y = 0.2\ s^{-1}$.

where, the unstable points found for the region $V_{GAPs} \in [810, 900]\ s^{-1}$ represent the oscillatory dynamics of the system. Outside this oscillatory regime, the system is monostable.
The dependence between the stationary X points and Y points can be found considering that

$$\frac{\partial[X]}{\partial t} = V^*_{GAPs}\left(\frac{[X]}{K_X+[X]}\right)\left(\frac{K_\alpha+\alpha[Y]}{K_\alpha+[Y]}\right)\left(\frac{[Y]}{K_{GAPs}+Y}\right) - V_{GEFs}\left(\frac{[X]}{K_{GEFs}+[X]}\right) + k - \lambda_X[X] = 0$$

$$= \frac{\partial[Y]}{\partial t} = V_{GEFs}\left(\frac{[X]}{K_{GEFs}+[X]}\right) - V^*_{GAPs}\left(\frac{[X]}{K_X+[X]}\right)\left(\frac{K_\alpha+\alpha[Y]}{K_\alpha+[Y]}\right)\left(\frac{[Y]}{K_{GAPs}+Y}\right) - \lambda_Y[Y] \Rightarrow$$

$$V_{GEFs}\left(\frac{[X]}{K_{GEFs}+[X]}\right) - V^*_{GAPs}\left(\frac{[X]}{K_X+[X]}\right)\left(\frac{K_\alpha+\alpha[Y]}{K_\alpha+[Y]}\right)\left(\frac{[Y]}{K_{GAPs}+Y}\right) = k - \lambda_X[X] = \lambda_Y[Y] \Rightarrow$$

$$k - \lambda_X[X] = \lambda_Y[Y] \Rightarrow [Y] = \frac{k - \lambda_X[X]}{\lambda_Y}$$

It is distinguishable how the new system is deprived of bistability after the addition of membrane association and dissociation rates. The hysteresis shape has become a sigmoidal curve, where the dynamics reaches a single final state. So, the emerged question is to figure out when exactly the bistability vanishes. Decreasing slowly the new added constants (k, λ_X and λ_Y) and plotting the stationary points while changing the parameter V^*_{GAPs} helps us to elucidate this issue.

- For $k \cdot n$, $\lambda_X \cdot n$ and $\lambda_Y \cdot n$ with $n = 0.1$:
  Now, the sigmoidal curve starts to resemble more to a step shape, analysing Fig.10. The system is monostable for all values of V^*_{GAPs}, except for the interval [920, 940] s^{-1}, where we find oscillations. This interval became smaller in comparison to the previous case with $n = 1$.

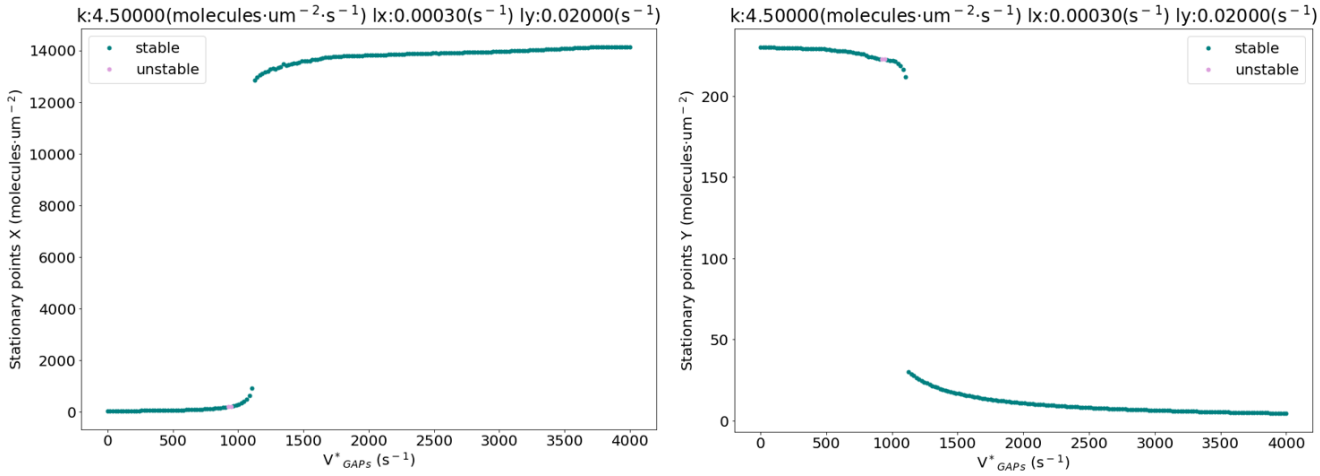

Figure 10: Stationary points of X (left) and Y (right) controlling V^*_{GAPs} and $k = 4.5\ molecules \cdot \mu m^{-2} s^{-1}$, $\lambda_X = 0.0003\ s^{-1}$ and $\lambda_Y = 0.02\ s^{-1}$.

- For $k \cdot n$, $\lambda_X \cdot n$ and $\lambda_Y \cdot n$ with $n = 0.01$:
  From Fig.11 a similar behaviour as before can be observed. However, the step shape is more pronounced than before and the oscillatory dynamics has vanished.

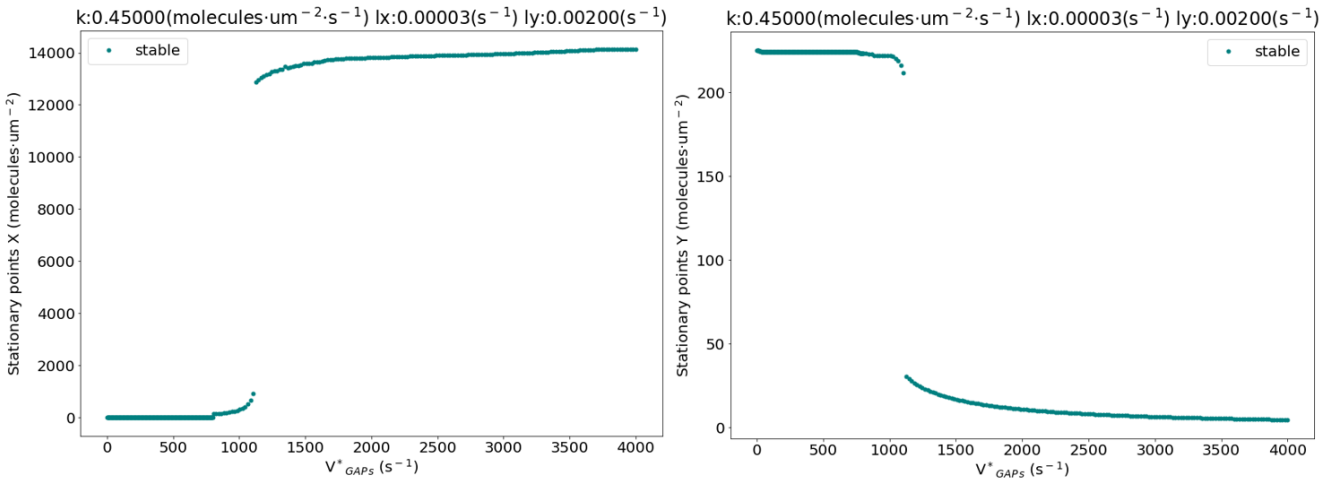

Figure 11: Stationary points of X (left) and Y (right) controlling V^*_{GAPs} and $k = 0.45\ molecules \cdot \mu m^{-2} s^{-1}$, $\lambda_X = 0.00003\ s^{-1}$ and $\lambda_Y = 0.002\ s^{-1}$.

- For $k \cdot n$, $\lambda_X \cdot n$ and $\lambda_Y \cdot n$ with $n \leq 0.0001$ and $n > 0.000001$, the system does not reach a stable state since the dissociation rates are $1 \cdot 10^7$ smaller than the parameters V^*_{GAPs} and V_{GEFs}. The system acts disregarding them as there was unlimited constant production and no dissociation.
- For $k \cdot n$, $\lambda_X \cdot n$ and $\lambda_Y \cdot n$ with $n = 0.000001$:
  The bistability is recovered since the values for k, λ_X and λ_Y are negligible in comparison to the other model parameters. For example, when V^*_{GAPs} and V_{GEFs} are of the order of magnitude 100, they are $\geq 1 \cdot 10^7$ than k, λ_X and λ_Y. Therefore, we return to the first conserved model with bistability, as it is depicted in Fig.12.

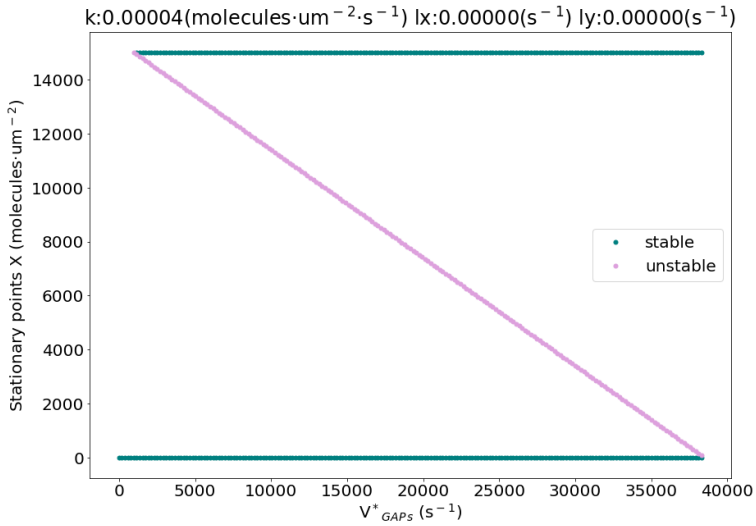

Figure 12: Stationary points of X varying V^*_{GAPs} and $k = 0.000045\ molecules \cdot \mu m^{-2} s^{-1}$, $\lambda_X = 0.0000\ s^{-1}$ and $\lambda_Y = 0.0000\ s^{-1}$.

In order to identify which parameters are responsible for low and high concentration states and for the oscillatory behavior, we add to the study two new cases. The first one will consider k, $\lambda_X \neq 0$ and $\lambda_Y = 0$ and the second one with k, $\lambda_Y \neq 0$ and $\lambda_X = 0$.
Completing the same procedure as previously for the rates k, $\lambda_X \neq 0$ and $\lambda_Y = 0$ we gather the subsequent results:

- For $k \cdot n$, $\lambda_X \cdot n$ and $\lambda_Y = 0$ with $n = 1$:

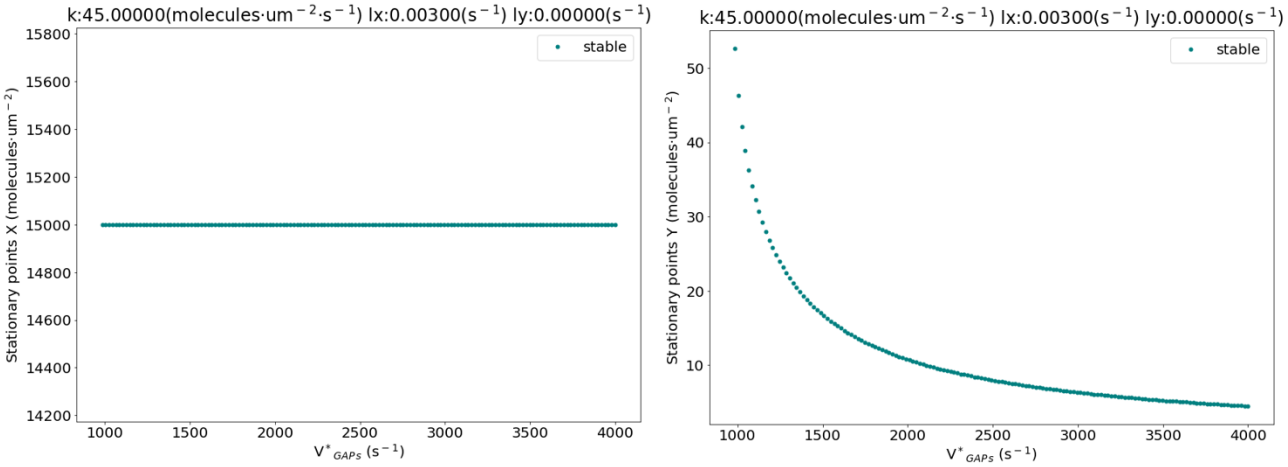

Figure 13: Stationary points of X (left) and Y (right) controlling V^*_{GAPs} and $k = 45\ molecules \cdot \mu m^{-2} s^{-1}$, $\lambda_X = 0.003\ s^{-1}$ and $\lambda_Y = 0.0\ s^{-1}$.

- For $k \cdot n$, $\lambda_X \cdot n$ and $\lambda_Y = 0$ with $n = 0.1$:

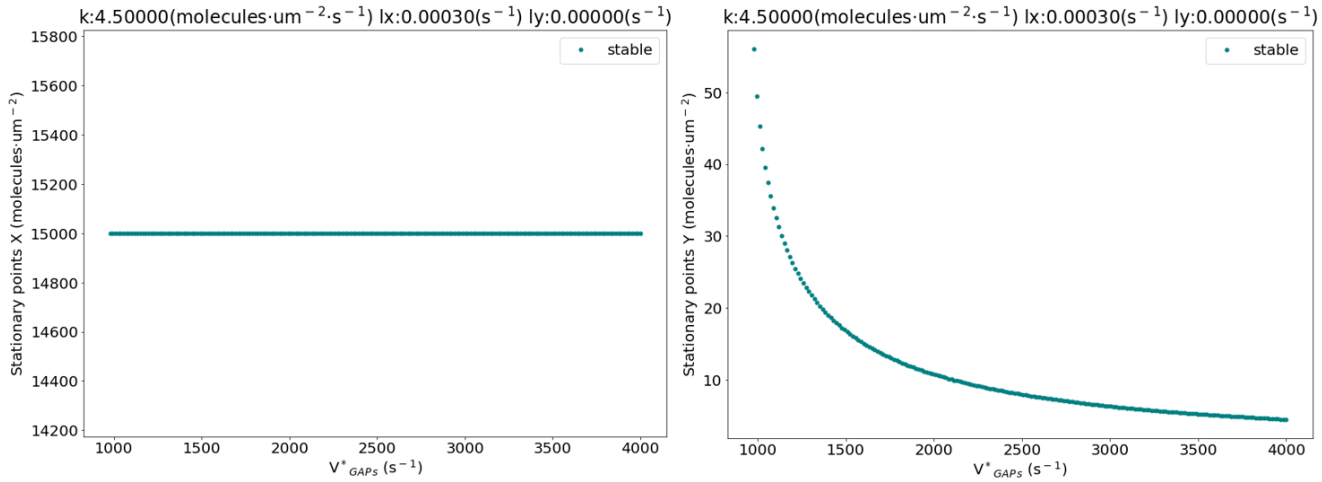

Figure 14: Stationary points of X (left) and Y (right) as a function of V^*_{GAPs} for $k = 4.5\ molecules \cdot \mu m^{-2} s^{-1}$, $\lambda_X = 0.0003\ s^{-1}$ and $\lambda_Y = 0.0\ s^{-1}$.

The figures Fig.13 and Fig.14 are in agreement with what is expected from the equations:

$$\frac{\partial[X]}{\partial t} = V^*_{GAPs}\left(\frac{[X]}{K_X+[X]}\right)\left(\frac{K_\alpha+\alpha[Y]}{K_\alpha+[Y]}\right)\left(\frac{[Y]}{K_{GAPs}+Y}\right) - V_{GEFs}\left(\frac{[X]}{K_{GEFs}+[X]}\right) + k - \lambda_X[X] = 0$$

$$= \frac{\partial[Y]}{\partial t} = V_{GEFs}\left(\frac{[X]}{K_{GEFs}+[X]}\right) - V^*_{GAPs}\left(\frac{[X]}{K_X+[X]}\right)\left(\frac{K_\alpha+\alpha[Y]}{K_\alpha+[Y]}\right)\left(\frac{[Y]}{K_{GAPs}+Y}\right) \Rightarrow$$

$$V_{GEFs}\left(\frac{[X]}{K_{GEFs}+[X]}\right) - V^*_{GAPs}\left(\frac{[X]}{K_X+[X]}\right)\left(\frac{K_\alpha+\alpha[Y]}{K_\alpha+[Y]}\right)\left(\frac{[Y]}{K_{GAPs}+Y}\right) = k - \lambda_X[X] = 0 \Rightarrow$$

$$k - \lambda_X[X] = 0 \Rightarrow [X] = \frac{k}{\lambda_X};$$

$$V_{GEFs}\left(\frac{[X]}{K_{GEFs}+[X]}\right) = V^*_{GAPs}\left(\frac{[X]}{K_X+[X]}\right)\left(\frac{K_\alpha+\alpha[Y]}{K_\alpha+[Y]}\right)\left(\frac{[Y]}{K_{GAPs}+Y}\right) \Rightarrow$$

$$\frac{V_{GEFs}}{V^*_{GAPs}}\left(\frac{[X]}{K_{GEFs}+[X]}\right)\left(\frac{K_X+[X]}{[X]}\right) = \left(\frac{K_\alpha+\alpha[Y]}{K_\alpha+[Y]}\right)\left(\frac{[Y]}{K_{GAPs}+Y}\right) \Rightarrow$$

$$\frac{const}{V^*_{GAPs}} = \frac{K_\alpha[Y]+\alpha[Y]^2}{K_\alpha K_{GAP}+K_\alpha[Y]+K_{GAP}[Y]+[Y]^2}$$

in which, we see that the [X] will be constant for any value of V^*_{GAPs} and [Y] will have a dependence on this parameter. The system does not have a final steady-solution for values of V^*_{GAPs} smaller than 1000, which causes the vanishing of oscillations.
For further cases when $n \geq 0.01$, the dynamics does not stabilizes to a final steady-state because the system behaves as having only membrane association rate k, as $\lambda_X \leq 3 \cdot 10^{-5}\ s^{-1}$, which is insignificant compared to the other equation parameters. The bistability is found for the same values as before: $n = 0.000001$ and the corresponding figure is Fig.15.

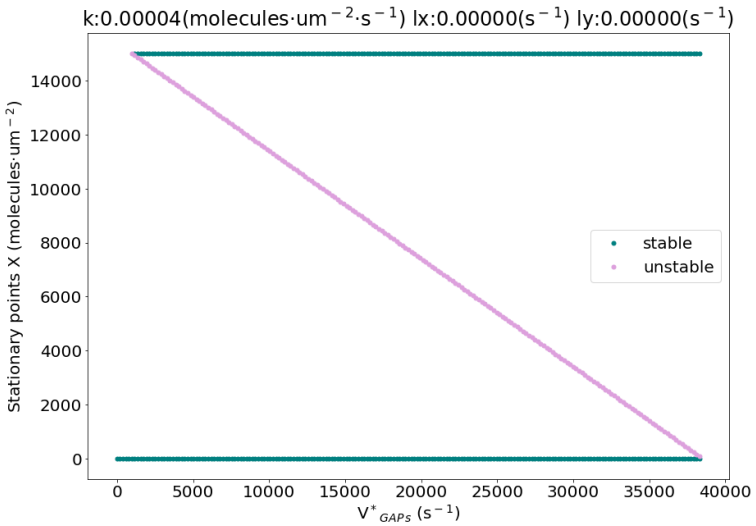

Figure 15: Stationary points of X for different V^*_{GAPs} and $k = 0.000045\ molecules \cdot \mu m^{-2} s^{-1}$, $\lambda_X = 0.0000\ s^{-1}$ and $\lambda_Y = 0.0000\ s^{-1}$.

The last case contemplates k, $\lambda_Y \neq 0$ and $\lambda_X = 0$, where we find the complementary steady-state solutions in order to achieve the total picture with k, λ_X and $\lambda_X \neq 0$.

- For $k \cdot n$, $\lambda_Y \cdot n$ and $\lambda_X = 0$ with $n = 1$:

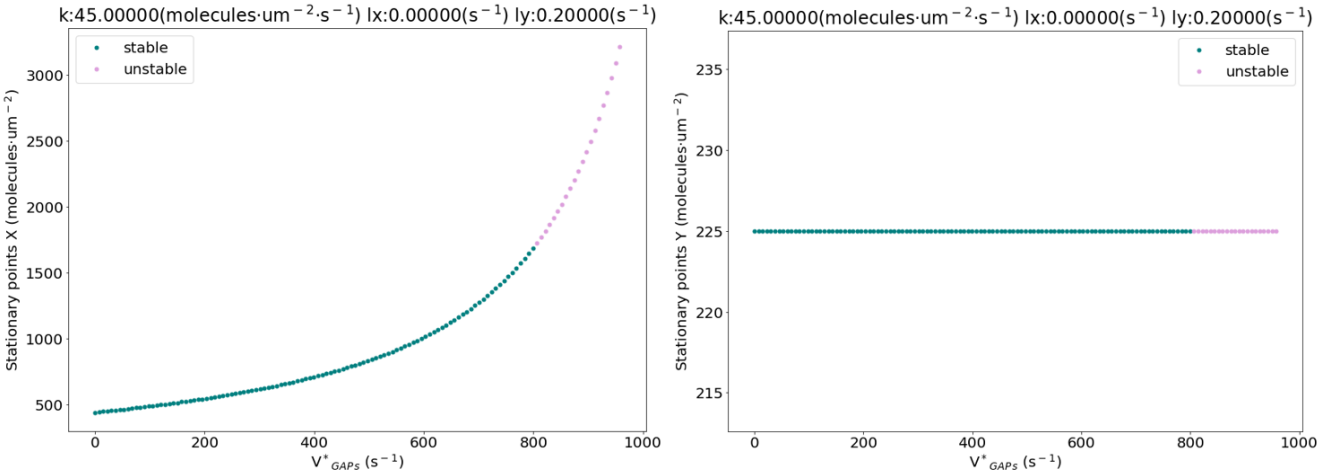

Figure 16: Stationary points of X (left) and Y (right) controlling V^*_{GAPs} and $k = 45\ molecules \cdot \mu m^{-2} s^{-1}$, $\lambda_X = 0.0\ s^{-1}$ and $\lambda_Y = 0.2\ s^{-1}$.

Fig. 16 shows us that the system steady-states only emerge for values of $V^*_{GAPs} \leq 950 s^{-1}$ and the interval of oscillations [800,950] s^{-1} is larger than for the complete model.

- For $k \cdot n$, $\lambda_Y \cdot n$ and $\lambda_X = 0$ with $n = 0.1$:
  From Fig. 17 we see how the interval of oscillations shrinks, as previously for the complete model when reducing the rates values.

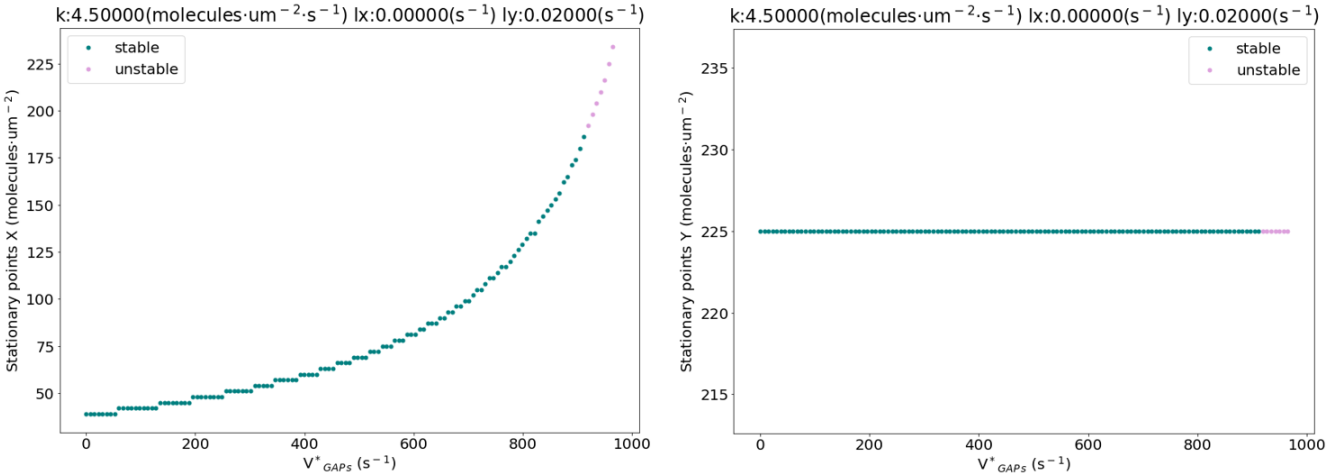

Figure 17: Stationary points of X (left) and Y (right) as a function V^*_{GAPs} and $k = 4.5\ molecules \cdot \mu m^{-2} s^{-1}$, $\lambda_X = 0.0\ s^{-1}$ and $\lambda_Y = 0.02\ s^{-1}$.

- For $k \cdot n$, $\lambda_Y \cdot n$ and $\lambda_X = 0$ with $n = 0.01$:
  Observing Fig.18, it is remarkable how the oscillations vanish and X values decrease describing the same curve as before.

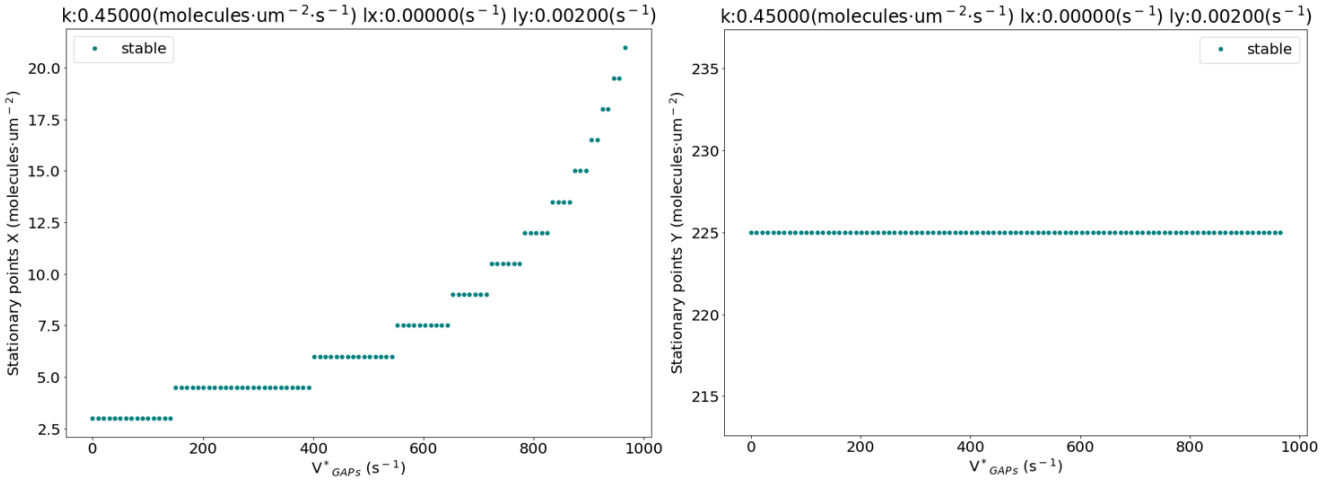

Figure 18: Stationary points of X (left) and Y (right) changing V^*_{GAPs} and $k = 0.45\ molecules \cdot \mu m^{-2} s^{-1}$, $\lambda_X = 0.0\ s^{-1}$ and $\lambda_Y = 0.002\ s^{-1}$.

- For $k \cdot n$, $\lambda_Y \cdot n$ and $\lambda_X = 0$ with $n = 0.001$:
  There are no oscillations and the stationary points of X are smaller than in the previous case, while Y stationary points are constant, in Fig.19.

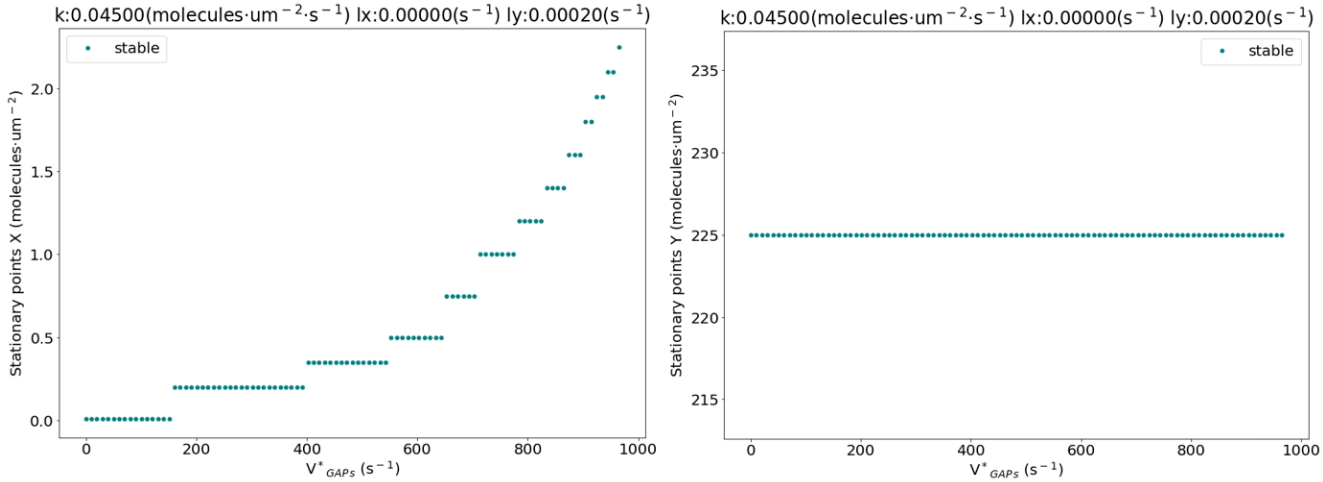

Figure 19: Stationary points of X (left) and Y (right) for different V^*_{GAPs} and $k = 0.045\ molecules \cdot \mu m^{-2} s^{-1}$, $\lambda_X = 0.0\ s^{-1}$ and $\lambda_Y = 0.0002\ s^{-1}$.

- For $k \cdot n$, $\lambda_X \cdot n$ and $\lambda_Y \cdot n$ with $n \leq 0.0001$ and $n > 0.000001$, the system does not stabilizes to a final solution for the formerly mentioned reasons of the order of magnitude.

In this case, the respective model tells us that:

$$\frac{\partial[X]}{\partial t} = V^*_{GAPs}\left(\frac{[X]}{K_X+[X]}\right)\left(\frac{K_\alpha+\alpha[Y]}{K_\alpha+[Y]}\right)\left(\frac{[Y]}{K_{GAPs}+Y}\right) - V_{GEFs}\left(\frac{[X]}{K_{GEFs}+[X]}\right)+k=0$$

$$=\frac{\partial[Y]}{\partial t} = V_{GEFs}\left(\frac{[X]}{K_{GEFs}+[X]}\right) - V^*_{GAPs}\left(\frac{[X]}{K_X+[X]}\right)\left(\frac{K_\alpha+\alpha[Y]}{K_\alpha+[Y]}\right)\left(\frac{[Y]}{K_{GAPs}+Y}\right) - \lambda_Y[Y] \Rightarrow$$

$$V_{GEFs}\left(\frac{[X]}{K_{GEFs}+[X]}\right) - V^*_{GAPs}\left(\frac{[X]}{K_X+[X]}\right)\left(\frac{K_\alpha+\alpha[Y]}{K_\alpha+[Y]}\right)\left(\frac{[Y]}{K_{GAPs}+Y}\right) = k = \lambda_Y[Y] \Rightarrow$$

$$k=\lambda_Y[Y]=0 \Rightarrow [Y]=\frac{k}{\lambda_Y};$$

$$k = V_{GEFs}\left(\frac{[X]}{K_{GEFs}+[X]}\right) - V^*_{GAPs}\left(\frac{[X]}{K_X+[X]}\right)\left(\frac{K_\alpha+\alpha[Y]}{K_\alpha+[Y]}\right)\left(\frac{[Y]}{K_{GAPs}+Y}\right) \Rightarrow$$

$$V_{GEFs}\left(\frac{[X]}{K_{GEFs}+[X]}\right) - V^*_{GAPs}\left(\frac{[X]}{K_X+[X]}\right)(const) = k$$

which is consistent with the above figures since [Y] is constant and [X] depends on the parameter V^*_{GAPs} and k. The bistability is also recovered for $n = 0.000001$ as earlier, displaying exactly the same behaviour as in Fig. 12 and Fig. 15.
Here the evidence for the complementary behavior of these two cases to give rise the complete model is manifested. The interactions between the association rate of Ras-GDP k and dissociation rate of Ras-GTP λ_Y provide the system with an oscillatory dynamics. We see how they are responsible also for low Ras-GDP ([X]) and high Ras-GTP ([Y]) concentration, and how k and λ_X are responsible for the opposite effect.

4.3 Model including GAPs dynamics without slaving

The latter analysis were done considering a fast dynamics and no diffusion for GAPs, however it is necessary to examine if such approximation is justified in the present system. Therefore, recovering the initial network for Ras signaling system without the feedback from PIP3 system and considering the simplified notation:

$$\frac{\partial[X]}{\partial t} = V_{GAPs}[Z]\left(\frac{[Y]}{K_{GAPs}+[Y]}\right) - V_{GEFs}\left(\frac{[X]}{K_{GEFs}+[X]}\right)+k-\lambda_X[X]+D\nabla^2[X] \tag{13}$$

$$\frac{\partial[Y]}{\partial t} = V_{GEFs}\left(\frac{[X]}{K_{GEFs}+[X]}\right) - V_{GAPs}[Z]\left(\frac{[Y]}{K_{GAPs}+[Y]}\right) - \lambda_Y[Y]+D\nabla^2[Y] \tag{14}$$

$$\frac{\partial[Z]}{\partial t} = V_{GAPs_{ass}}[Z]_{cyt}\left(\frac{[X]}{K_X+[X]}\right)\left(\frac{K_\alpha+\alpha[Y]}{K_\alpha+[Y]}\right) - \lambda_Z[Z]+D\nabla^2[Z] \tag{15}$$

in which, the cytosolic concentration is given by $[Z]_{cyt} = [Z]_{total} - \chi\overline{[Z]}$. Here, we find the parameter V_{GAPs} different from V^*_{GAPs} of the GAPs slaved dynamics, where it is defined as $V_{GAPs}\frac{V_{GAPs_{ass}}[Z]_{cyt}}{\lambda_Z}$. The scheme reproducing the system properties for the model of Eqs. (13-15) is shown in Fig.20.

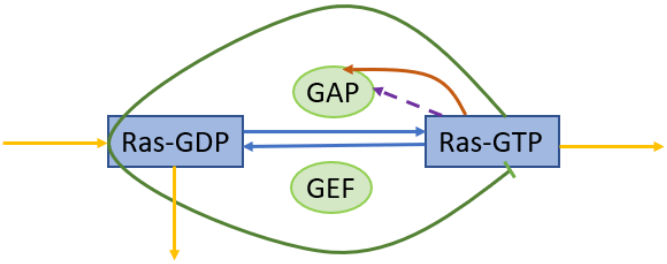

Figure 20: Scheme for Ras signaling network including GAPs dynamics described by Eqs. (13-15).

The laplacian discretization in one dimension is: $\nabla^2 C = \frac{C(x+dx)+C(x-dx)-2\cdot C(x)}{dx^2}$ with C corresponding to Ras-GDP, Ras-GTP or GAPs. For the numerical integration, a simple Euler method is employed. The time and spatial steps are detailed in Table 1, see appendices.
Previously, we found that the system displays an oscillatory dynamics for certain values of the parameter V^*_{GAPs} in the no-conserved model, in particular for the interval [800, 900] s^{-1} when $n = 1$. In order to check if we obtain the same behavior with the no-slaved GAPs dynamics (Fig.21 and Fig.22), we choose for example two values of V_{GAPs} and compare to the earlier obtained results. For the simulations performed the parameters k, λ_X, λ_Y, K_X, K_α, α, K_{GAPs} and K_{GEFs} adopt the values established in Table 2 (appendices).

- For $V_{GAPs} = 10\ s^{-1}$, which is approximately equal to consider in GAPs slaved dynamics $V^*_{GAPs} \equiv V_{GAPs}\frac{V_{GAPs_{ass}}[Z]_{cyt}}{\lambda_Z} \approx 10 \cdot \frac{1300}{1.2} \cdot (0.1 - 0.001 \cdot 22) = 845\ s^{-1}$. We have already seen that for this value we obtain an oscillatory dynamics in the previous model. The respective values are listed in the appendices (see Table2) and the average is computed with the 1D deterministic simulations of this model. The oscillations are not exactly the same because the GAPs slaved dynamics is considered as an approximation.

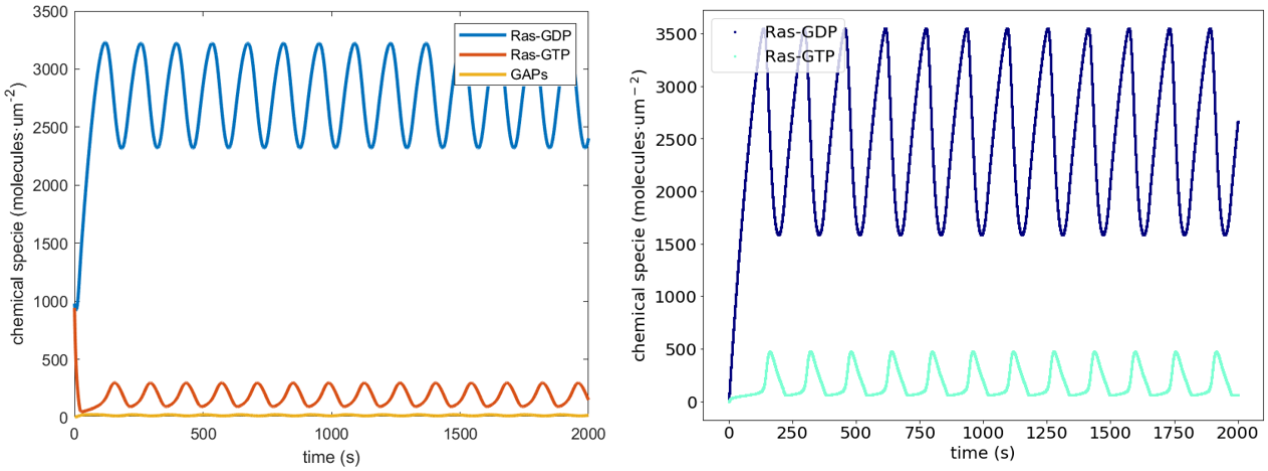

Figure 21: Temporal evolution of Ras-GDP, Ras-GTP and GAPs for $V_{GAPs} = 10\ s^{-1}$ and $V_{GEFs} = 400\ s^{-1}$ according to Eqs. (13-15), with the initial condition defined in [3] (left). Temporal evolution of Ras-GDP and Ras-GTP for the Eqs. (11-12) for $V^*_{GAPs} = 845\ s^{-1}$ and $V_{GEFs} = 400\ s^{-1}$ (right).

- For $V_{GAPs} = 16\ s^{-1} \Rightarrow V^*_{GAPs} \equiv V_{GAPs}\frac{V_{GAPs_{ass}}[Z]_{cyt}}{\lambda_Z} \approx 16 \cdot \frac{1300}{1.2} \cdot (0.1 - 0.001 \cdot 40) = 1040\ s^{-1}$ in GAPs slaved dynamics model, we have a single stable steady-state shown in Fig.22:

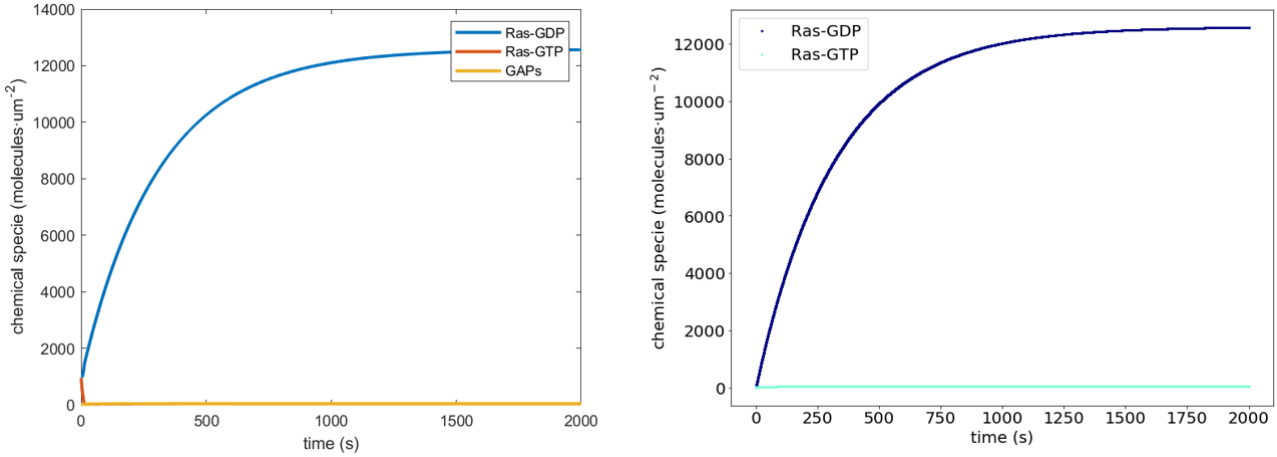

Figure 22: Temporal evolution of Ras-GDP (X), Ras-GTP (Y) and GAPs (Z) for $V_{GAPs} = 16\ s^{-1}$ and $V_{GEFs} = 400\ s^{-1}$ according to (13-15), with the initial condition defined in [3] (left). Temporal evolution of Ras-GDP and Ras-GTP for the Eqs. (11-12) for $V^*_{GAPs} = 1040\ s^{-1}$ and $V_{GEFs} = 400\ s^{-1}$ (right).

The global oscillations can also emerge when we vary V_{GEFs} parameter, which corresponds to the regulation of Ras activation. Increasing V_{GEFs} with the other parameters constant, the system passes through an oscillatory regime as it remains proven in Fig.23 and Fig.24.

- For $V_{GEFs} = 550\ s^{-1}$, the interactions between the active and inactive Ras give rise to global oscillations:

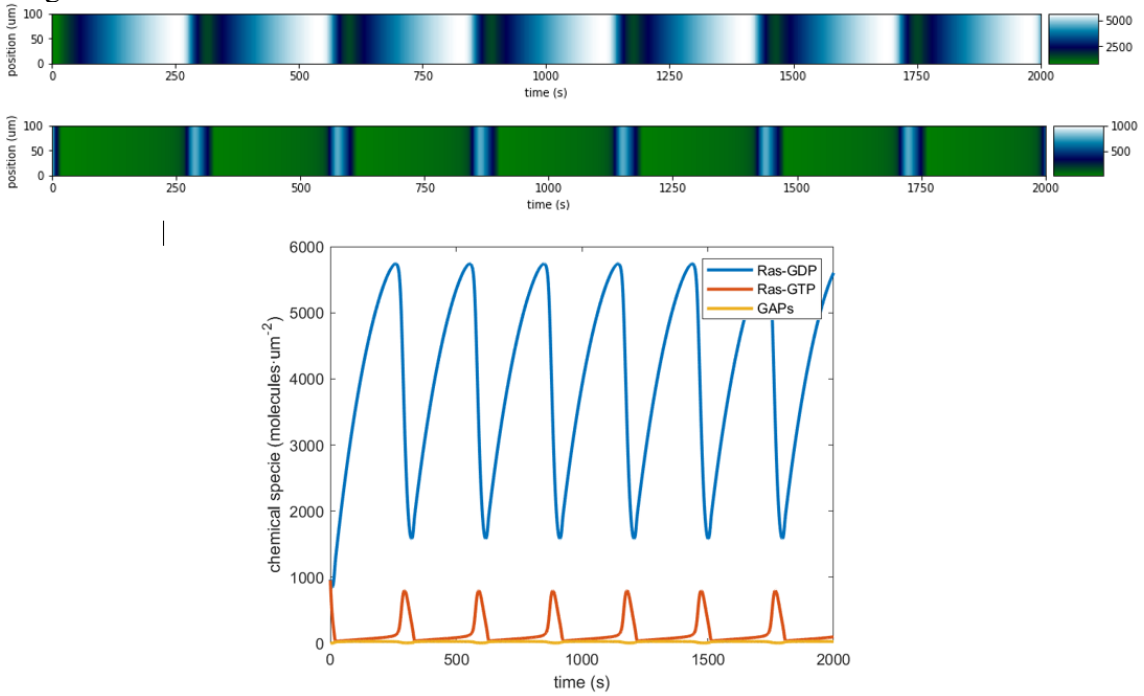

Figure 23: Spatiotemporal simulation for Ras-GDP (X) (top) and for Ras-GTP (Y) (middle) and temporal simulation of (13-15) (bottom) for $V_{GAPs} = 16\ s^{-1}$ and $V_{GEFs} = 550\ s^{-1}$, with initial conditions defined in Table 2.

- For $V_{GEFs} = 650\ s^{-1}$, the system is still displaying global oscillations with a greater frequency than in the previous case. This indicates us that there is a dependence between the period of oscillations and the parameter V_{GEFs}, which will be discuss later.

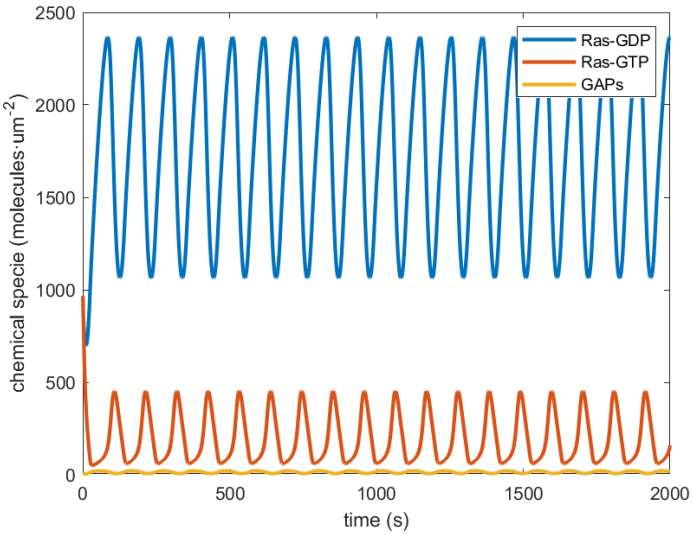

Figure 24: Zero dimensional simulation of (13-15) for Ras-GDP (X), Ras-GTP (Y) and GAPs (Z) when $V_{GAPs} = 16\ s^{-1}$ and $V_{GEFs} = 650\ s^{-1}$.

- For $V_{GEFs} = 900\ s^{-1}$, the stability of the final state is recovered and the system becomes monostable again, observing the temporal simulation from Fig.25.

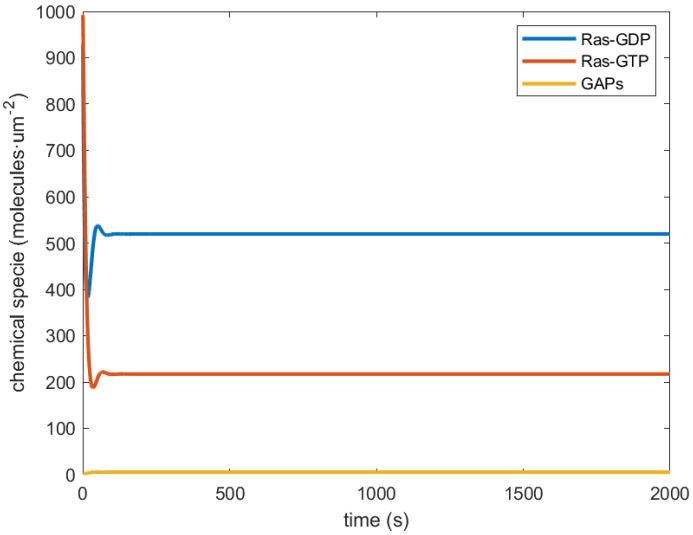

Figure 25: Temporal evolution of Eqs. (13-15) for Ras-GDP (X), Ras-GTP (Y) and GAPs (Z) when $V_{GAPs} = 16 s^{-1}$ and $V_{GEFs} = 900\ s^{-1}$.

GAPs dynamics is positively regulated by the cytosolic concentration which in turn is directly related to the total GAPs concentration available for the reaction. An oscillatory pattern appears whether controlling the total GAPs concentration ($[GAPs]_{total}$) and the parameter V_{GEFs}. When the $[GAPs]_{total}$ is smaller than 0.05 μM, there is not enough GAPs concentration to trigger the oscillatory dynamics of the system. Above this limit the system exhibits an oscillatory behaviour, when regulating the parameter V_{GEFs}. Therefore, a phase diagram presented in Fig.26, adjusting these two factors, may be a very helpful tool to our study of Ras oscillatory dynamics.

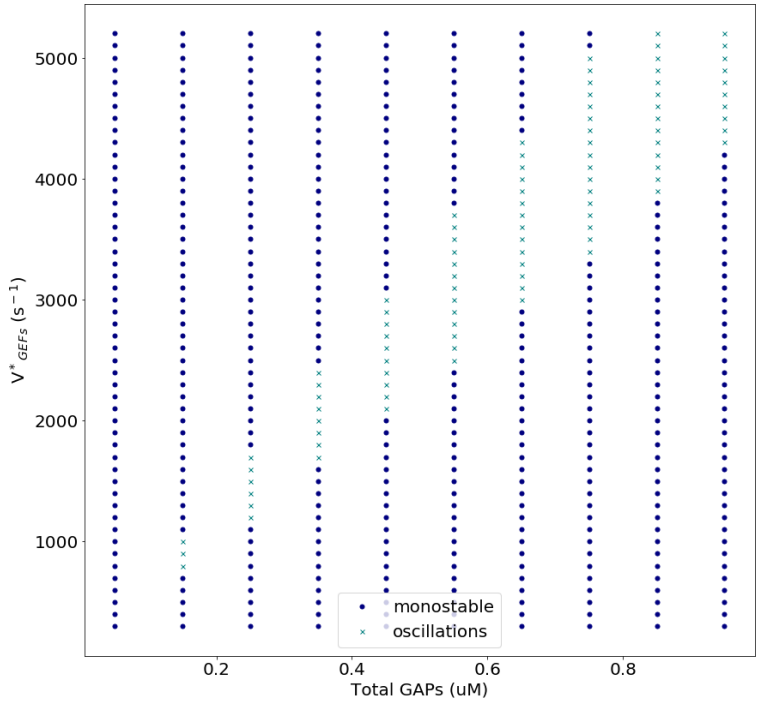

Figure 26: Phase diagram of the system dynamics controlling the parameters V_{GEFs} and $[GAPs]_{total}$, for the model of Eqs. (13-15).

The signaling pathways involved in chemotaxis can be interpreted as excitable systems [3, 15]. Fukushima et al. found that Ras dynamics displays excitable characteristics and that the signal transduction to trigger cell motility happens at this stage. Its main contribution to cell migration stands on the spontaneous symmetry breaking. An excitable system has only one stable steady-state solution and due to the nonlinear interactions it displays complex behaviour when the stimuli exceeds the characteristic threshold. To enlighten the evidence for Ras excitability described with the former model, a spatio-termporal figure for $V_{GEFs} = 500\ s^{-1}$ is presented in Fig.27 for different boundary conditions and performing deterministic and stochastic simulation in one dimension:

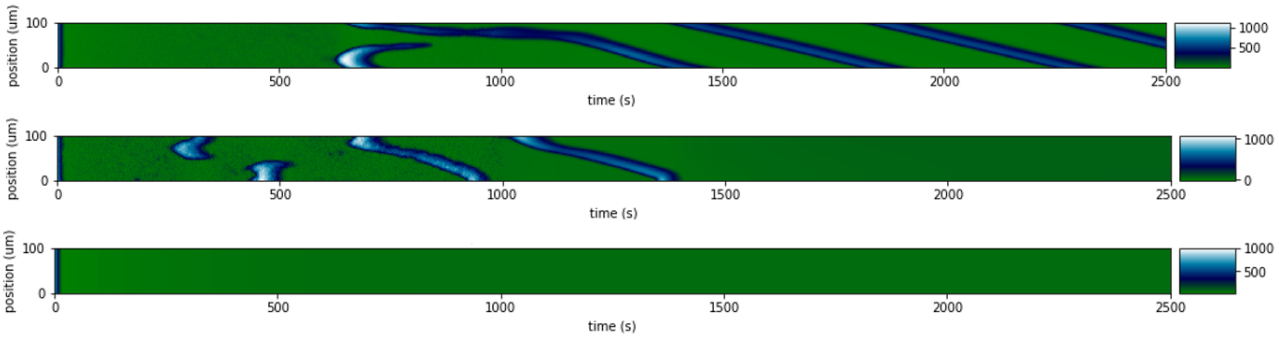

Figure 27: Spatiotemporal evolution for Ras-GTP considering periodic boundary conditions and performing stochastic simulation until $t = 1000s$ and deterministic afterwards (top), applying no-flux boundary conditions with stochastic integration up to $t = 1000s$ and deterministic afterwards (middle) and purely deterministic simulation with no-flux boundary conditions (bottom).

Therefore, we see how a travelling wave is generated and how it propagates due to Ras excitability properties, when applying periodic boundary conditions. Whether employing no-flux boundary conditions, the wave cease propagating when it finishes at one side of the system and it does not appear anymore. To remark the excitable properties of Ras network, one may compare the previous plot to a purely deterministic simulation. It is useful to search whether we find global oscillations that may be confused with excitable dynamics when applying perturbation to the system, e.g. stochastic integration. The subsequent figures show us that there are no global oscillations present in the system. Thus, the Ras signaling system displays excitable dynamics for $V_{GEFs} = 500\ s^{-1}$, without the feedback from PIP3 system, as it remains exemplified in Fig.27.

A stochastic simulation was performed until $t = 1000s$, employing the Chemical Langevin equation (CLE) for Ras-GTP, Ras-GDP and GAPs dynamics. For $t > 1000s$ and $t \leq 2500s$, the simulation is deterministic. Spatial-stochastic effects have a relevant contribution in the biochemical networks involved in intracellular processes and other processes at different biological scales. Whether the chemical species are an intermediate number of particles, the internal noise is described as a white Gaussian noise using the CLE. Therefore, for the present system we use a phenomenological mesoscopic approach. Eqs. (13-15) in the framework of the Chemical Langevin Equations are

$$\frac{\partial [X]}{\partial t} = V_{GAPs}[Z]\left(\frac{[Y]}{K_{GAPs}+[Y]}\right) - V_{GEFs}\left(\frac{[X]}{K_{GEFs}+[X]}\right) + k - \lambda_X[X] + D\nabla^2[X]$$
$$+\sqrt{|\, V_{GAPs}[Z]\left(\frac{[Y]}{K_{GAPs}+[Y]}\right)\,|}\cdot\xi_1(t) - \sqrt{|\, V_{GEFs}\left(\frac{[X]}{K_{GEFs}+[X]}\right)\,|}\cdot\xi_2(t) - \sqrt{|\,\lambda_X[X]\,|}\cdot\xi_3(t) \tag{16}$$

$$\frac{\partial [Y]}{\partial t} = V_{GEFs}\left(\frac{[X]}{K_{GEFs}+[X]}\right) - V_{GAPs}[Z]\left(\frac{[Y]}{K_{GAPs}+[Y]}\right) - \lambda_Y[Y] + D\nabla^2[Y]$$
$$+\sqrt{|\, V_{GEFs}\left(\frac{[X]}{K_{GEFs}+[X]}\right)\,|}\cdot\xi_2(t) - \sqrt{|\, V_{GAPs}[Z]\left(\frac{[Y]}{K_{GAPs}+[Y]}\right)\,|}\cdot\xi_1(t) - \sqrt{|\,\lambda_Y[Y]\,|}\cdot\xi_4(t) \tag{17}$$

$$\frac{\partial[Z]}{\partial t} = V_{GAPs_{ass}}[Z]_{cyt}\left(\frac{[X]}{K_X+[X]}\right)\left(\frac{K_\alpha+\alpha[Y]}{K_\alpha+[Y]}\right) - \lambda_Z[Z] + D\nabla^2[Z]$$
$$+\sqrt{|\, V_{GAPs_{ass}}[Z]_{cyt}\left(\frac{[X]}{K_X+[X]}\right)\left(\frac{K_\alpha+\alpha[Y]}{K_\alpha+[Y]}\right)|}\cdot\xi_5(t) - \sqrt{|\,\lambda_Z[Z]\,|}\cdot\xi_6(t) \tag{18}$$

The oscillatory pattern for this system begins at $V_{GEFs} = 530\ s^{-1}$, shown in Fig.28. The period decreases as V_{GEFs} increases till a certain limit, where the system becomes monostable again.

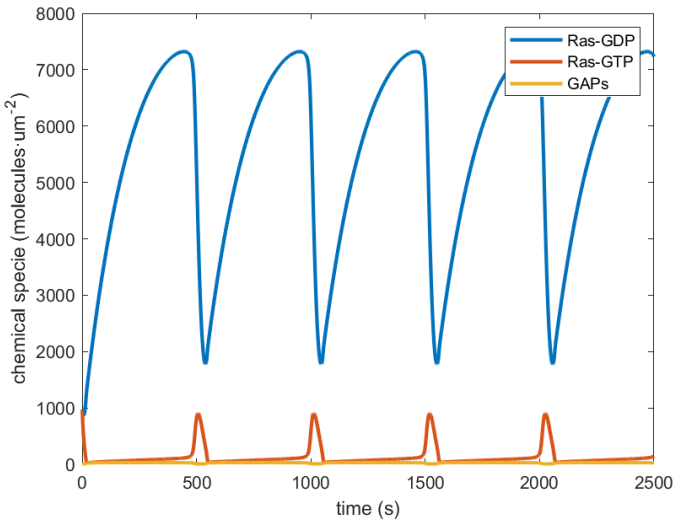

Figure 28: Temporal evolution of deterministic Eqs [13-15] for Ras-GDP (X), Ras-GTP (Y) and GAPs (Z) when $V_{GAPs} = 16\ s^{-1}$ and $V_{GEFs} = 530\ s^{-1}$.

From Fig. 23 and Fig. 24, we can observe how the period decreases when V_{GEFs} is enhanced, maintaining the other parameters constant. Hence, the relation between these two factors is:

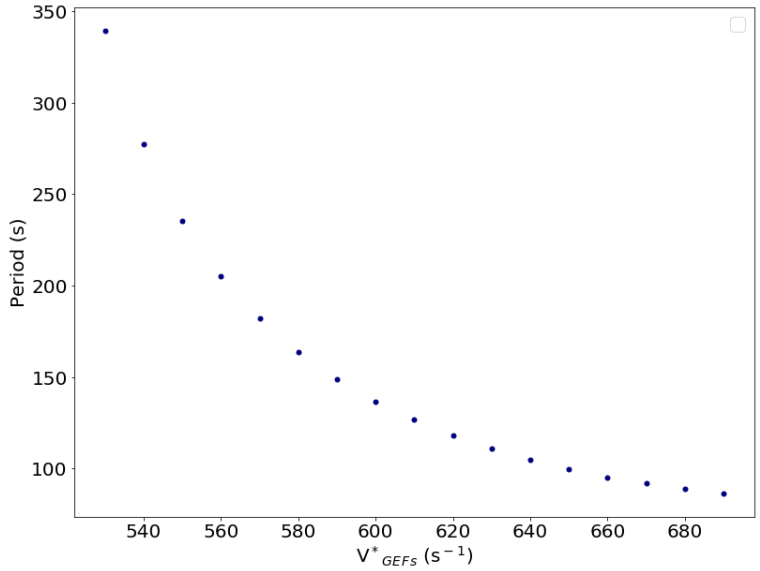

Figure 29: The dependence between the period of oscillations and the parameter V_{GEFs}.

Therefore, Ras signaling system described by the Eqs. (13-15) displays monostable, excitable and oscillatory behavior as a function of the maximum reaction rate for Ras activation, V_{GEFs}, illustrated in Fig.30 .

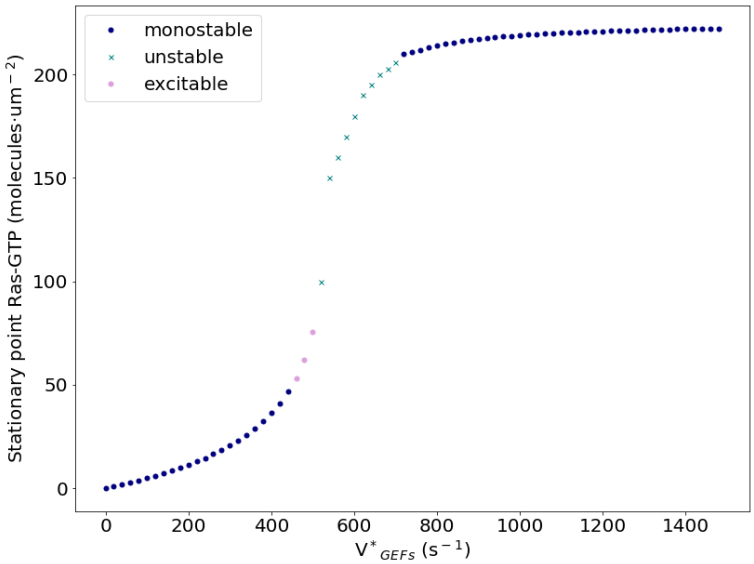

Figure 30: The phase space of Ras signaling network. The dynamics can be monostable, excitable or unstable depending on the value of V_{GEFs}. The unstable points give rise to an oscillatory pattern in the system.

4.4 Combined model for Ras and PIP3 signaling networks

The model developed by Fukushima et al. (2019) contemplates a coupling between the Ras signaling system and bistable PIP3 signaling system incorporated at the positive regulation of Ras, R_{GEF}, as can be seen in Eq. (3). Thus, the combined model introduced in [3] is formed by two coupled signaling networks: one part presented at the beginning of the project Eqs. (1-6) which stands for the Ras excitable signaling system is:

$$\frac{\partial[Ras-GDP]}{\partial t} = R_{GAP} - R_{GEF} + k - \lambda_{Ras-GDP}[Ras-GDP] + D\nabla^2[Ras-GDP]$$

$$\frac{\partial[Ras-GTP]}{\partial t} = R_{GEF} - R_{GAP} - \lambda_{Ras-GTP}[Ras-GTP] + D\nabla^2[Ras-GTP]$$

$$R_{GEF} = \left(V_{GEFs} + \frac{V_{feedback}[PIP3]}{K_{PIP3}+[PIP3]}\right)\left(\frac{[Ras-GDP]}{K_{GEFs}+[Ras-GDP]}\right)$$

$$R_{GAP} = V_{GAPs}[GAPs]\left(\frac{[Ras-GTP]}{K_{GAPs}+[Ras-GTP]}\right)$$

$$\frac{\partial[GAPs]}{\partial t} = V_{GAPs_{ass}}[GAPs]_{cyt}\left(\frac{[Ras-GDP]}{K_{Ras-GDP}+[Ras-GDP]}\right)\left(\frac{K_\alpha+\alpha[Ras-GTP]}{K_\alpha+[Ras-GTP]}\right)$$
$$-\lambda_{GAPs}[GAPs] + D\nabla^2[GAPs]$$

$$[GAPs]_{cyt} = [GAPs]_{total} - \chi\overline{[GAPs]}$$

And the second model is represented by the reaction diffusion equations reproducing the bistable dynamics of PIP3:

$$\frac{\partial[PIP3]}{\partial t} = R_{PI3K} - R_{PTEN} - \lambda_{PIP3}[PIP3] + D\nabla^2[PIP3] \tag{19}$$

$$\frac{\partial[PIP2]}{\partial t} = R_{PTEN} - R_{PI3K} + \lambda_{PIP3}[PIP3] + D\nabla^2[PIP2] \tag{20}$$

$$\overline{[PIP3]} + \overline{[PIP2]} = [PIP]_{total} \tag{21}$$

$$R_{PI3K} = V_{PI3K}\left(\frac{[PIP2]}{K_{PI3K} + [PIP2]}\right) \tag{22}$$

$$R_{PTEN} = V_{PTEN}[PTEN]\left(\frac{[PIP3]}{K_{PTEN} + [PIP3]}\right) \tag{23}$$

$$[PI3K] = \beta[Ras - GTP] \tag{24}$$

$$\frac{\partial[PTEN]}{\partial t} = -R_{PTEN} + V_{PTEN_{ass}}[PTEN]_{cyt}\left(\frac{[PIP2]}{K_{PIP2} + [PIP2]}\right) + D\nabla^2[PTEN] \tag{25}$$

$$[PTEN]_{cyt} = [PTEN]_{total} - \chi\overline{[PTEN]} \tag{26}$$

Equations (19) and (20) describe the PIP3 and PIP2 dynamics evolution, where PIP3 is generated from the PIP2 phosphorylation reaction catalyzed by PI3K and the opposite reaction of dephosphorylation is carried out by PTEN. These reactions are of the type Michaelis-Menten enzymatic reactions with a maximum reaction rate (V_{PI3K} and V_{PTEN}) and a Michaelis constant (K_{PI3K} and K_{PTEN}). The sum of PIP3 and PIP2 averaged concentrations is taken as a constant Eq. (21). The membrane translocation of PI3K is proportional to Ras-GTP, and by considering the membrane association rate of PI3K (β), Eq. (24) designates the activation of PI3K by Ras-GTP. PTEN dynamics is governed by two factors, Eq. (25): PIP3 excludes PTEN from the membrane, which results in a mutual exclusion on the membrane and PIP2 helps the cytosolic PTEN to associate to the membrane, where the cytosolic concentration of PTEN is the rest of the total concentration and the surface concentration multiplied by a constant that converts it to a volume concentration, Eq. (26) [3, 30].
A scheme for Ras and PIP3 dynamics, designated by Eqs. (1-6) and (19-26) is portrayed in Fig.31.

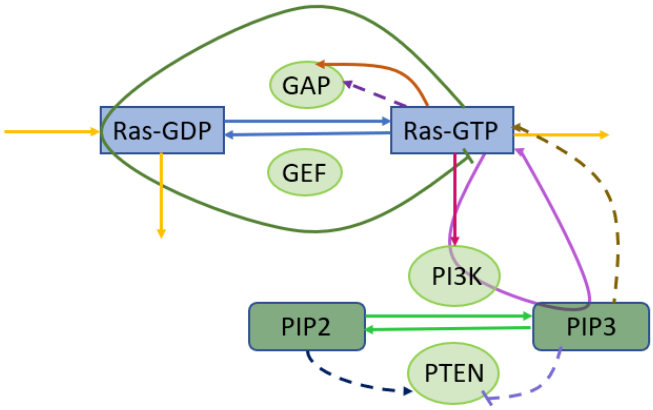

Figure 31: Scheme of the coupled Ras-PIP3 system.

The activation of Ras has an additional term which is given by the feedback from PIP3, that is also expressed as a MM-type enzymatic reaction. As it was already proven with the model for Ras without PIP3 feedback, Ras waves generation is regardless the downstream signaling pathways. Thus, it is interesting to observe which is the repercussion of this feedback on Ras excitability properties and waves generation. The new phase space from Fig.32 for the coupled model shows us that the excitability properties and the oscillatory dynamics start for a smaller value of V_{GEFs} since there is an additional term coming from the PIP3 feedback which makes the total effective maximum reaction rate higher. Moreover, the curve exhibit an identical sigmoidal shape with a shift to the left compared to the model without feedback, as can be observed in Fig.32.

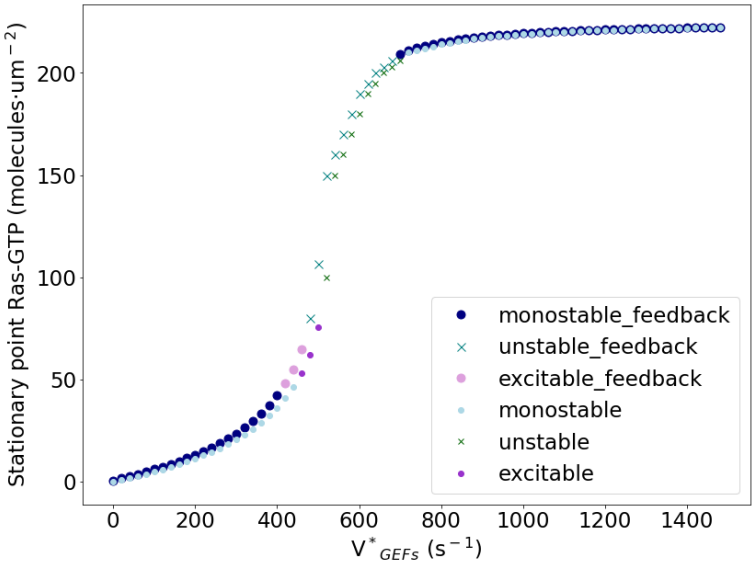

Figure 32: The phase space of the coupled Ras-PIP3 system changing the value of V_{GEFs}, $V_{feedback} = 25\ s^{-1}$ which corresponds to the curve displaced to the left (larger points labeled with "_feedback"). The phase space of Ras signaling system without feedback corresponding to the curve with smaller marks, presented also in Fig.30.

Therefore, such a feedback only lowers the value of the maximum reaction rate of Ras basal activity for excitable or oscillatory properties. However, PIP3 needs the activation from Ras in order to generate waves since the phosphorylation reaction depends on PI3K concentration, which is proportional to Ras-GTP. Hence, a similar phase space is obtained in both cases (Fig. 30-Fig. 32): without the feedback mechanism, Ras network is excitable starting with $V_{GEFs} = 460\ s^{-1}$, and if PIP3 regulates positively Ras activation, the excitable dynamics appears for $V_{GEFs} = 420\ s^{-1}$ and the oscillatory patterns for $V_{GEFs} = 480\ s^{-1}$.
Moreover, the period of oscillations dependence on the parameter V_{GEFs} does not change much either in Fig.33. We see that global oscillations emerge for a smaller V_{GEFs}, as it was expected.

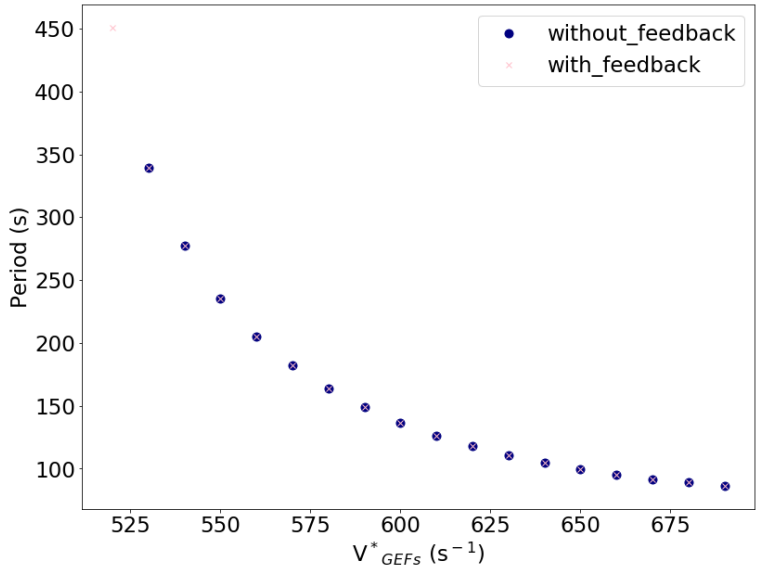

Figure 33: The period of oscillations as a function of the parameter V_{GEFs}, with $V_{feedback} = 25\ s^{-1}$ are represented by the pink marks. The period of oscillations as a function of the parameter V_{GEFs}, with $V_{feedback} = 0\ s^{-1}$, are the blue dots, displayed in Fig.29. The curves are overlapped except for the first point, indicating that for the feedback mechanisms the oscillations start earlier.

To see the relevance of PIP3 feedback and the activation from Ras-GTP, the following deterministic simulations were performed. The initial conditions are the final values from stochastic simulations and after a certain time PI3K activity was cut off. First of all, periodic boundary conditions were considered to analyze wave propagation for distinct values of V_{GEFs}:

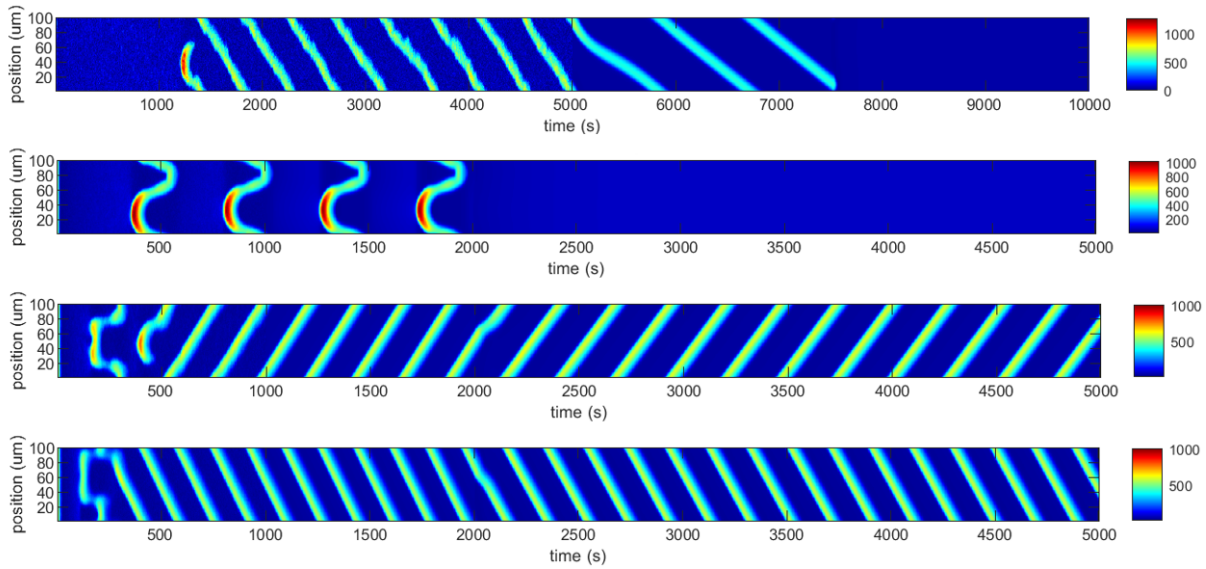

Figure 34: Spatiotemporal simulations for Ras-GTP for $V_{GEFs} = 450\ s^{-1}$ (first), $V_{GEFs} = 500\ s^{-1}$ (second), $V_{GEFs} = 550\ s^{-1}$ (third) and $V_{GEFs} = 600\ s^{-1}$ (fourth), for $V_{feedback} = 25\ s^{-1}$ and periodic boundary conditions. At the beginning we have stochastic integration up to $t = 5000s$ for the first case and up to $t = 1000s$ for the other cases, afterwards we have deterministic simulations.

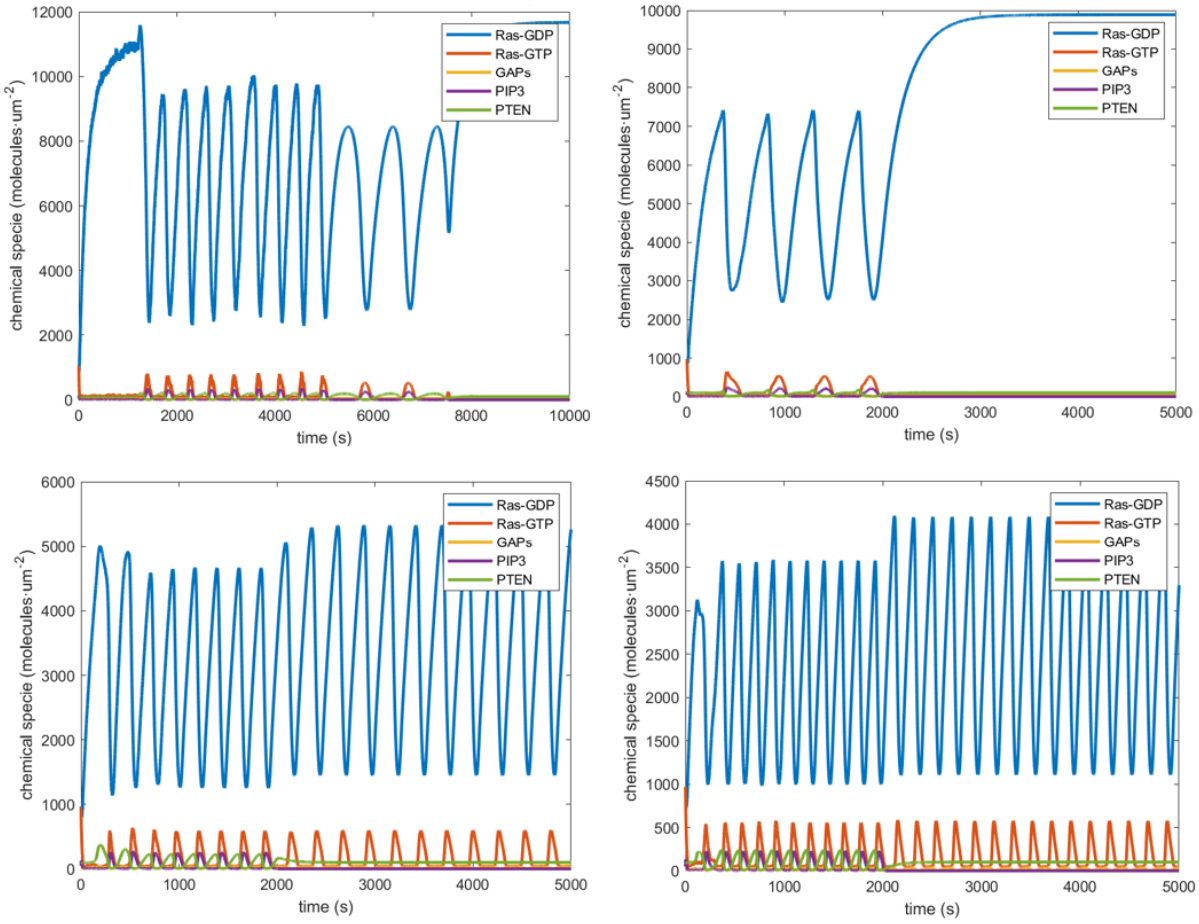

Figure 35: Temporal evolution for Ras-GDP, Ras-GTP, GAPs, PIP3 and PTEN for $V_{GEFs} = 450s^{-1}$ (top-left), $V_{GEFs} = 500s^{-1}$ (top-right), $V_{GEFs} = 550s^{-1}$ (bottom-left) and $V_{GEFs} = 600s^{-1}$ (bottom-right).

- For $V_{GEFs} = 450\ s^{-1}$, in Fig.34 first plot: Stochastic integration was performed up to $t = 5000s$, followed by deterministic integration. PIP3 and PTEN waves stop when V_{PI3K} is inhibited at $t = 7500\ s$ as can be seen the respective temporal evolution figure (Fig.35), because Ras does not activate PIP3 anymore. Also, Ras waves cease because there is no more positive feedback from PIP3.
- For $V_{GEFs} = 500\ s^{-1}$, in Fig.34 second plot: The spatiotemporal stochastic simulation for Ras-GTP stops at $t \leq 1000\ s$. The deterministic integration is employed for $t > 1000$ and for $t \geq 2000\ s$ V_{PI3K} is inhibited, where all waves stop the propagation.
- For $V_{GEFs} = 550\ s^{-1}$, in Fig.34 third plot: The spatiotemporal stochastic simulation for Ras-GTP is used for $t \leq 1000\ s$ and deterministic simulation for $t > 1000$. For $t \geq 2000\ s$ V_{PI3K} is inhibited, where PIP3 waves disappear, but Ras waves are still propagating.
- For $V_{GEFs} = 600\ s^{-1}$, in Fig.34 fourth plot: The same integration approach is used in here.

Therefore, for $V_{GEFs} = 450\ s^{-1}$ and $500\ s^{-1}$, the waves cease when PI3K activity is maintained to zero. However, for bigger values of the maximum reaction rate V_{GEFs}, Ras waves still propagate with a small readjustment right after PI3K inhibition. To ensure Ras excitable and oscillatory dynamics, the same simulations were implemented with no-flux boundary conditions.

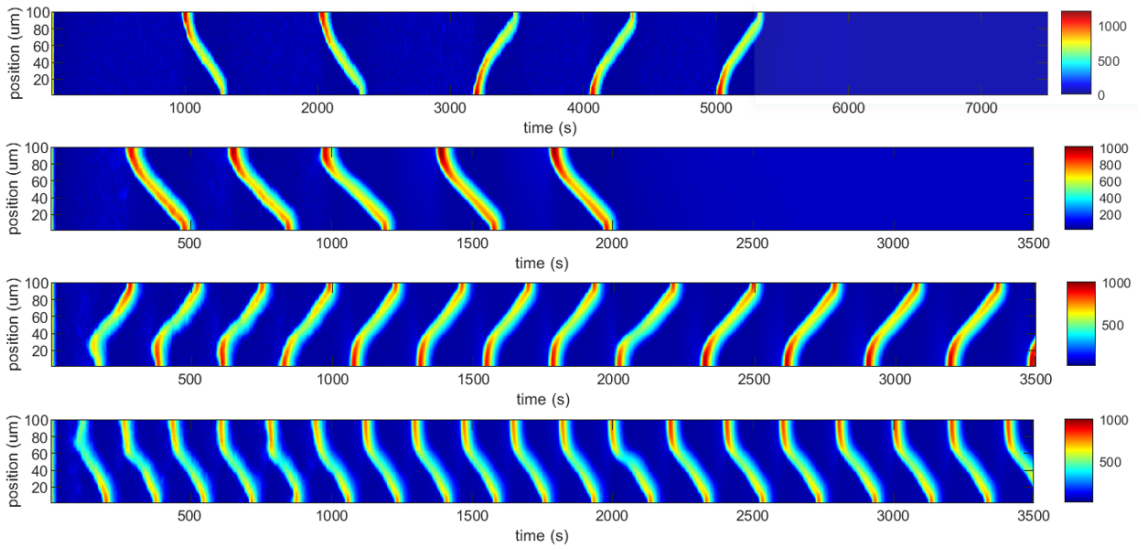

Figure 36: Spatiotemporal simulations for Ras-GTP for $V_{GEFs} = 450\ s^{-1}$ (first), $V_{GEFs} = 500\ s^{-1}$ (second), $V_{GEFs} = 550\ s^{-1}$ (third) and $V_{GEFs} = 600\ s^{-1}$ (fourth), for $V_{feedback} = 25\ s^{-1}$ and no-flux boundary conditions.

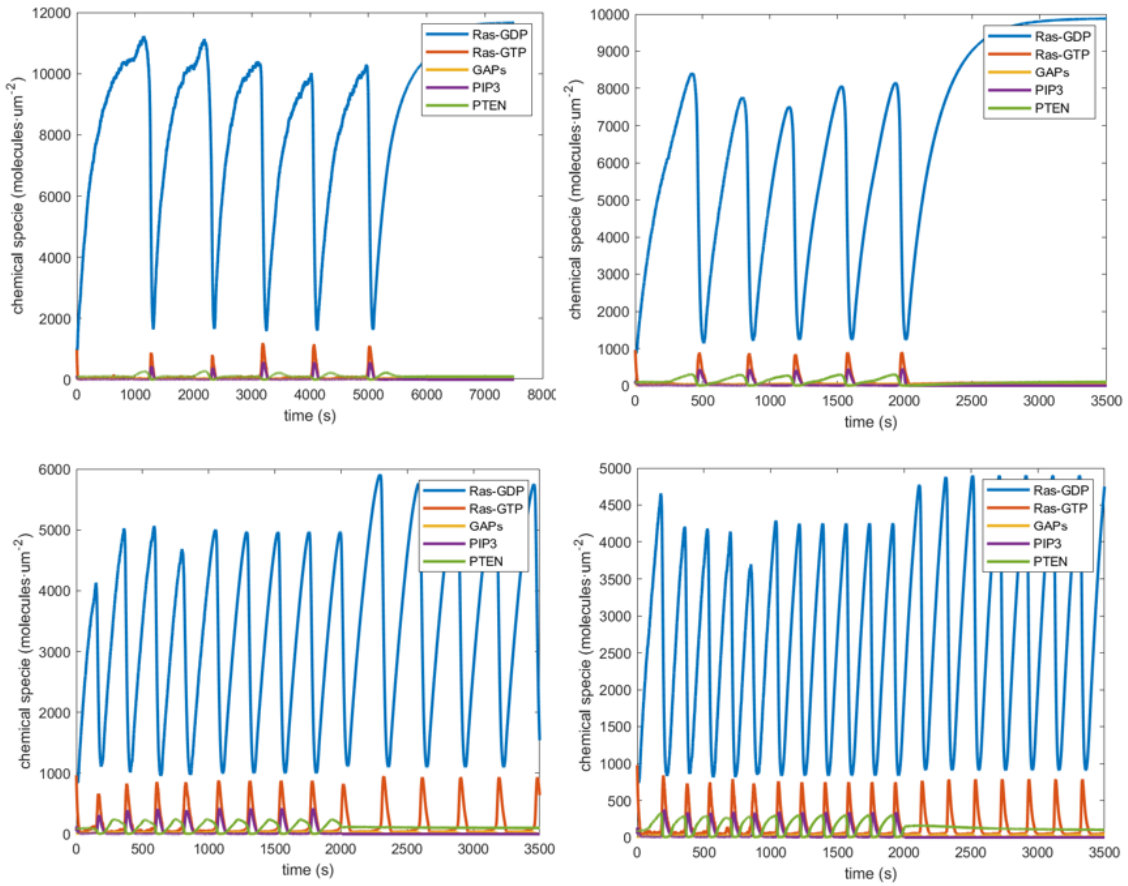

Figure 37: Temporal evolution for the coupled system for Ras-GDP, Ras-GTP, GAPs, PIP3 and PTEN when $V_{GAPs} = 16\ s^{-1}$ and $V_{GEFs} = 450\ s^{-1}$ (top-left), $V_{GEFs} = 500\ s^{-1}$ (top-right), $V_{GEFs} = 550\ s^{-1}$ (bottom-left) and $V_{GEFs} = 600\ s^{-1}$ (bottom-right), for $V_{feedback} = 25\ s^{-1}$.

- For $V_{GEFs} = 450\ s^{-1}$, in Fig.36 first plot: The stochastic simulation for Ras-GTP is implemented for $t \leq 5000\ s$, and the deterministic simulation for $t > 5000$. V_{PI3K} is inhibited for $t \geq 6000\ s$.
- For $V_{GEFs} = 500\ s^{-1}$, in Fig.36 second plot: The stochastic integration for Ras-GTP is when $t \leq 1000\ s$ and the deterministic simulation starts with $t = 1000$ and for $t \geq 2000\ s$ V_{PI3K} is inhibited.
- For $V_{GEFs} = 550\ s^{-1}$ and for $V_{GEFs} = 600\ s^{-1}$, in Fig.36 third and fourth figure: The same approach as before is applied.

For $V_{GEFs} = 450\ s^{-1}$ and $V_{feedback} = 25\ s^{-1}$ we have an excitable dynamics for Ras system because once the wave finishes at one side it does not appear anymore, with no-flux boundary conditions. Although, for the other values, the system is oscillatory since the waves keep appearing and propagate periodically, as it was established with the phase space.

4.5 Excitability in two dimensions

The preceding results can be broadened when considering the diffusion term for two spatial dimensions. Therefore, the laplacian of a certain concentration of protein or phospholipid C will have the following form, where the domain of integration is discretized in small 2D squares of size dx:

$$\nabla^2 C = \frac{C(x+dx,y) + C(x-dx,y) + C(x,y+dx) + C(x,y-dx) - 4 \cdot C(x,y)}{dx^2} \tag{27}$$

To reproduce the cell size, the domain of integration is taken as a square of 100 grids, with $dx = 0.314 \mu m$ (Table 1), which is obtained by considering a cell radius of $R_o = 5 \mu m$. Therefore, the integration algorithms for the studied model are extended to two dimensions considering Eq.(27) for the respective protein, enzyme and phospholipid concentrations.
The propagation of a Ras wave for a two-dimensional excitable system is studied for the model without the PIP3 feedback regulation Eqs. (13-15), Fig.38 and Fig.39, and for the combined model Eqs. (1-6), (19-26) with the feedback loop, Fig.40 and Fig.41. Such information is helpful to determine whether the system dynamics displays excitability.

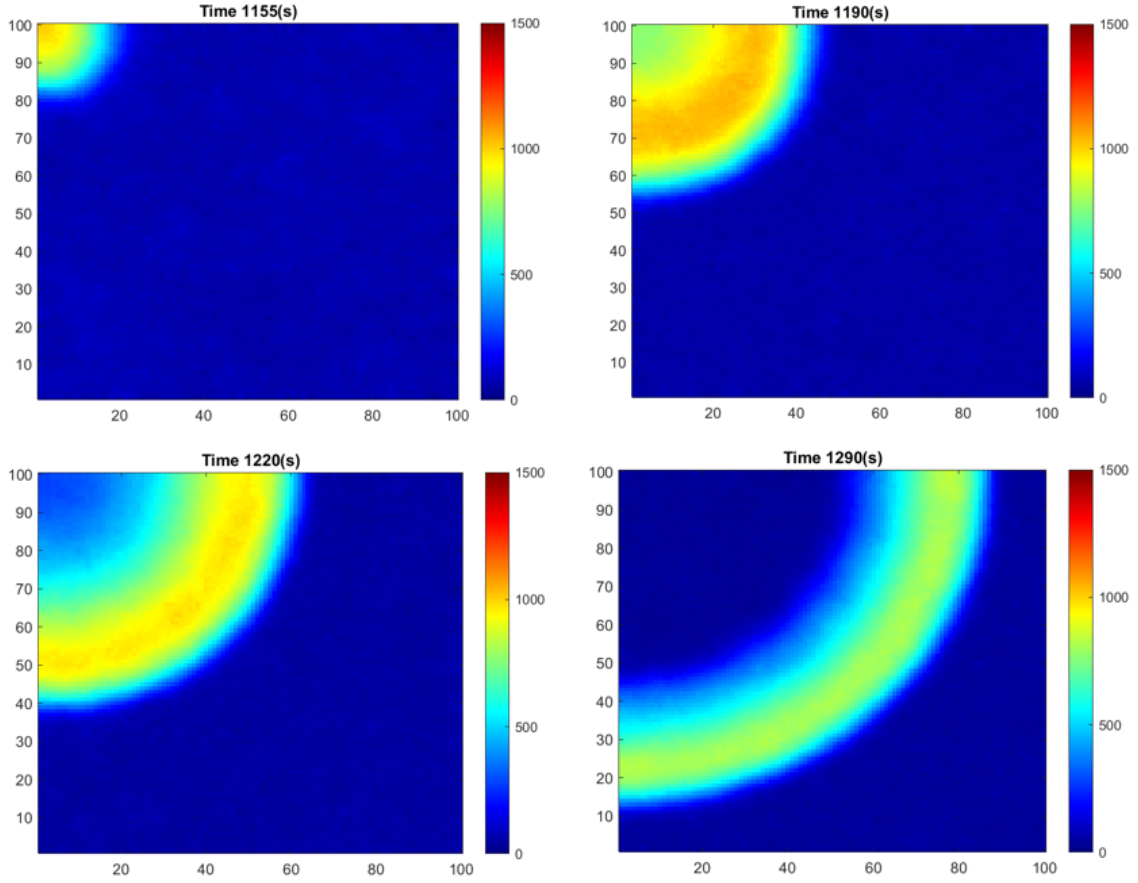

Figure 38: Stochastic simulation of Ras-GTP wave expansion $V_{GEFs} = 500\ s^{-1}$ and $V_{feedback} = 0\ s^{-1}$, for several times, when $t = 1155s$ (top-left), $t = 1190s$ (top-right), $t = 1220s$ (bottom-left) and $t = 1290s$ (bottom-right), with no-flux boundary conditions.

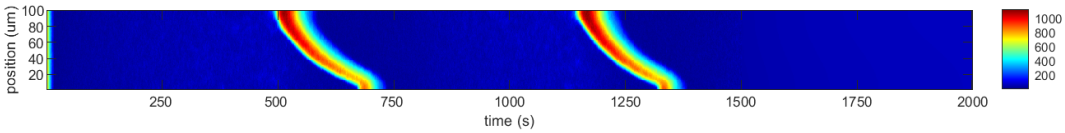

Figure 39: Profile in the y direction of the stochastic simulation of Ras-GTP until $t = 1500s$ for $V_{GEFs} = 500\ s^{-1}$ and $V_{feedback} = 0\ s^{-1}$ and deterministic afterwards, with no-flux boundary conditions.

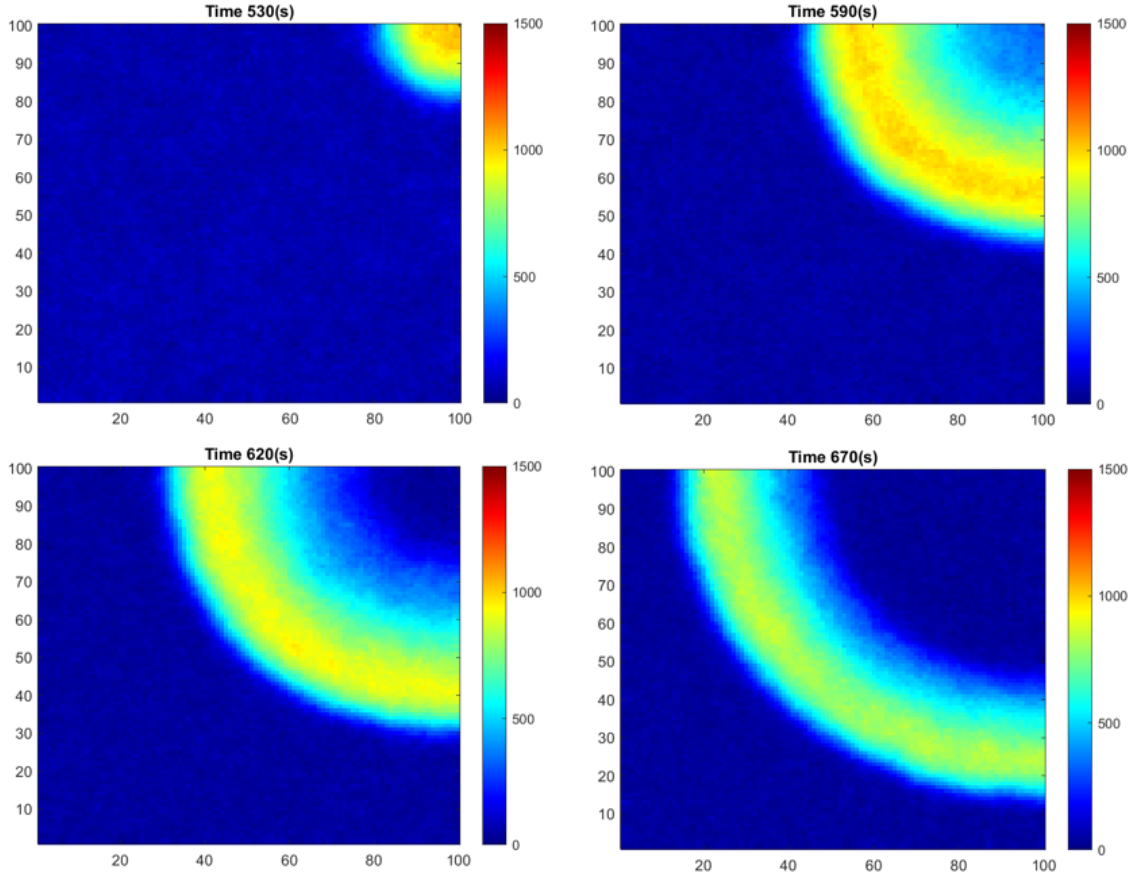

Figure 40: Stochastic simulation of Ras-GTP wave expansion $V_{GEFs} = 470\ s^{-1}$ and $V_{feedback} = 25\ s^{-1}$, for various times, when $t = 530s$ (top-left), $t = 590s$ (top-right), $t = 620s$ (bottom-left) and $t = 670s$ (bottom-right), with no-flux boundary conditions.

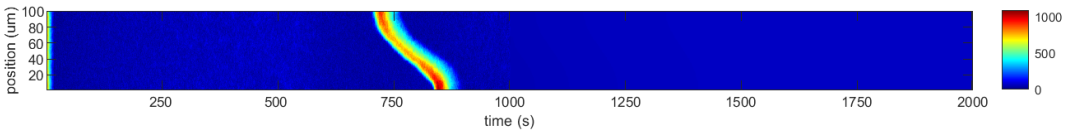

Figure 41: Profile in the y direction of the stochastic simulation of Ras-GTP until $t = 1000s$ for $V_{GEFs} = 470\ s^{-1}$ and $V_{feedback} = 25\ s^{-1}$ and deterministic afterwards, with no-flux boundary conditions.

For this reason, the excitability in two dimensions remains proven for Ras signaling network in both cases: without PIP3 feedback and with this positive regulation loop from PIP3. The stochastic integration of the internal noise represents a perturbation that generates a wave. This wave propagation illustrates the excitable characteristics of the system. It can be perturbed again and a new wave can emerge after a certain refractory period. Without noise and applying no-flux boundary conditions, the system does not manifest waves for the selected values of V_{GEFs} as can be observed in the figures of the system profile in the y direction, Fig. 39 and Fig. 41. Thus, the confirmation of an excitable behaviour for the given values is achieved.

4.6 Coupling with an auxiliary phase field

A recently new approach is used to reproduce the cell morphodynamics for the amoeboid motion, known as an auxiliary dynamic phase field. The eukaryotic cells moving with crawling motion are considered as a moving boundary problem, so it is useful to employ an additional field to maintain the no-flux boundary conditions at the edges. The phase field acts as an order parameter describing the cell area: it is $\phi = 1$ inside the circular domain and $\phi = 0$ outside the cell. At the cell membrane it takes an intermediate value $\phi = 0.5$ to contemplate a smooth progression from the inner cell to the exterior. Now, all the variables of concentration are multiplied by ϕ. The phase field initial configuration is a circular domain of radius $R_o = 5\mu m$ and boundary width ε, where ϕ takes the following values

$$r = \sqrt{(x-x_o)^2 + (y-y_o)^2}$$
$$\phi(x,y) = 0.5 + 0.5 \cdot tanh\frac{(R_o - r)}{(dx \cdot \varepsilon)}$$

where x and y correspond to the points of a square lattice of $L = 160$ and x_o and y_o represent the center of the domain. The evolution of a dynamic phase field is governed by the domain shape and is controlled by different contributions as surface tension, volume conservation, active tension and friction force:

$$\tau\frac{\partial\phi}{\partial t} = \gamma(\nabla^2\phi - \frac{G'(\phi)}{\varepsilon^2}) - \beta\left(\int\phi dx - A_o\right)|\nabla\phi| + \alpha[PIP3]|\nabla\phi| \tag{28}$$

The first element from Eq. (28) stands for the surface tension force and can be obtained from the surface energy of a cell with a perimeter L implemented as

$$H_{ten} = \gamma L = \gamma\int\left(\frac{\varepsilon}{2}|\nabla\phi|^2 + \frac{G(\phi)}{\varepsilon}\right)$$

in here $\gamma = 2.0\ pN$ and represents the surface tension parameter, the edge width is $\varepsilon = 3.5 \cdot dx$ and $G(\phi) = 18\phi^2(1-\phi)^2$ describes a double well potential with two minimum points at $\phi = 0$ and $\phi = 1$. Looking for the line density of surface tension force from the area density F^*_{ten}

$$F_{ten} = \frac{F^*_{ten}}{\varepsilon|\nabla\phi|^2} = -\frac{\delta H_{ten}}{\delta\phi}\frac{\nabla\phi}{\varepsilon|\nabla\phi|^2} = -\gamma\left(\nabla^2\phi - \frac{G'(\phi)}{\varepsilon^2}\right)\frac{\nabla\phi}{|\nabla\phi|^2} \tag{29}$$

The second component represents a restriction for the volume conservation, where $\beta = 5.066$ $pN\ \mu m^{-3}$ is the total area constraint parameter and $A_o = \pi \cdot {R_o}^2$ is the cell area:

$$F_{area} = \beta\left(\int\phi dx - A_o\right)\frac{\nabla\phi}{|\nabla\phi|} \tag{30}$$

The last part corresponds to the coupling of the phase field with PIP3 production in order to model how the cell generates a force for the directed motility. The phase field is linked to this phospholipid because it is responsible for the actin polymerization, which enables the cytoskeletal remodeling and protrusion activities leading to directed cell movement. The parameter describing the active tension is $\alpha = 0.03\ pN\ \mu m^{-1}$.

Finally, at the quasi-steady state the total force has to be approximately zero. Considering the friction force $F = -\tau v$, where the time scale of membrane dynamics is $\tau = 2.0\ pN\ s\ \mu m^{-2}$, and that the phase field evolution can be derived as $\frac{\partial \phi}{\partial t} = -v\nabla\phi$, the Eq. (28) is obtained.

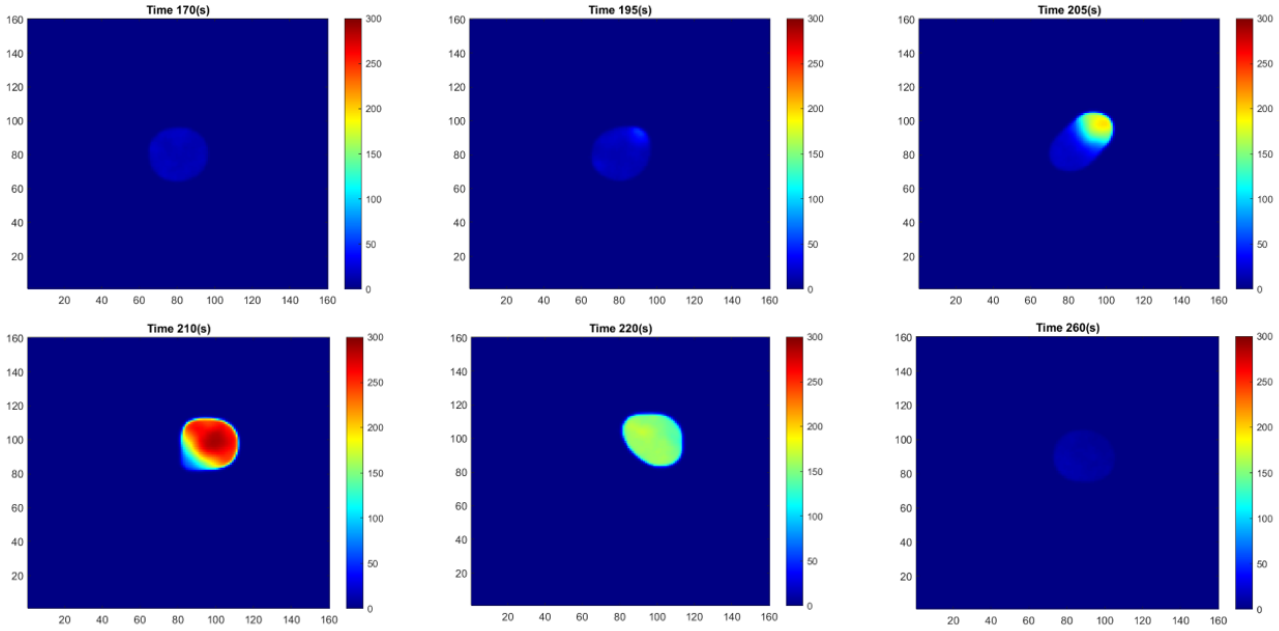

Figure 42: Simulation of the cell dynamics when applying an auxiliary phase field, for several times. The brightest spot at the leading edge indicates PIP3 concentration, which points the direction towards the cell is migrating.

Due to perturbations, the system is excited at the up-left edge, where a wave is generated, observing Fig.42, the second snapshot. During the propagation of such a wave, the circular domain imitating a cell moves towards the direction where PIP3 concentration is higher. Therefore, we can see how this accumulation creates a force capable of moving the cell to a preferential direction, in Fig.42, the third snapshot. In Fig.42, the last snapshot shows a cell which recovers its circular shape after the wave's passing and a refractory period and it is ready for a new excitation which will produce the required locomotion.

5 Conclusions and future development

At larger scales than the order magnitude 1 *mm*, passing from unicellular to pluricellular organisms, evolution and the laws of complexity and self-organization allowed us and other species to develop sensory organs in order to perceive the surrounding environment. We identify and interpret the immediate stimuli to survive, feed, interact, learn and carry out many vital functions due to our senses. So, the sensory faculty is essential to sustain oneself. But, what about the machinery responsible for sensing located at single cell level or unicellular organisms?
An extremely complex network capable of the interpretation and transduction of external cues is necessary to achieve an effective sensing of the neighbouring medium, at a single cell scale. The center of attention lies on the chemotaxis in the model organism *Dictyostelium discoideum*. The mechanisms portraying these phenomena are described in the present study in order to built a model disposed to simulate the spatiotemporal dynamics of the chemical species involved.
In the first place, an excitable signaling system is necessary for the symmetry breaking of the cell. The Ras signaling network, which plays a central role in the asymmetric signal generation, is pictured as an excitable system to reproduce the intended characteristics and activates the downstream signaling pathways, as PIP3. The latter system displays a bistable dynamics since it can exhibit two possible stationary states. A complete model combining these two signaling networks is employed for the symmetry breaking during cellular decision-making processes leading to cell polarity and locomotion. Such a network is built from a simple conserved model similar to the classical phosphorylation-dephosphorylation system adding gradually new feedbacks, protein dynamics and other elements shattering the conservation.
A relevant point is how Ras excitable system displays waves generation, regardless the downstream signaling pathways, as PIP3. The PIP3 positive feedback only lowers the value of the maximum activation reaction rate of Ras basal activity for excitable or oscillatory properties. Still and all, the final model of an excitable network for Ras and a bistable for PIP3 (equations 1-6 and 19-26) coupled to a phase field with an initial circular domain can reproduce the directed cell migration during chemotaxis. Summarizing, the main aspects to keep in mind from this study are:

- The regions of bistability, excitability and oscillations related to Ras signaling system are found and studied in detailed.
- A stochastic model is built in order to perform more realistic simulations for the symmetry breaking, cell polarity and cell migration of *Dictyostelium discoideum*.
- The phase field method is employed to characterise the cell movement.

Dictyostelium discoideum is not the only organism employing chemotaxis, other eukaryotic cells also avail themselves with chemotaxis, as neutrophils, which need this mechanism to migrate towards the inflammation spots, to chase pathogens [31]. Also, chemotaxis is considered an important factor in morphogenesis, metastasis, oncogenesis, atherosclerosis, arthritis, periodontitis, psoriasis among others [1, 2, 31, 32]. Therefore, I would like to remark the importance of a model describing cells ability for a directed motion, which is transcendental to understand better this process with many vital implications.
For a future research, it would be beneficial for medicine to gain more specific insights into Ras excitable signaling network, in particular the factors responsible for the threshold or the

activation. In addition, this model should be extended to neutrophils and complemented with experimental data. A model considering more elements from the downstream signaling pathways can be designed in order to describe better the actin waves and cytoskeletal reorganization. Besides, this model can be used to study how cortical waves drive fission of motile cells. Another interesting application might be to employ this model to engineer self-propeled vesicles, in the area of soft robotics, with the aim of controlling their locomotion.

References

[1] Atsuo T. Sasaki and Richard A.. Firtel. Regulation of chemotaxis by the orchestrated activation of Ras, PI3K and TOR. *European Journal of Cell Biology*, 85, 2006.

[2] Arjan Kortholt, Peter J.M., and J.M. Van Haastert. Highlighting the role of Ras and Rap during Dictyostelium chemotaxis. *Cellular Signaling*, 20, 1415-1422, 2008.

[3] Seiya Fukushima, Satomi Matsuoka, and Masahiro Ueda. Excitable dynamics of Ras triggers spontaneous symmetry breaking of PIP3 signaling in motile cells. *Journal of Cell Science*, 132, 2019.

[4] Rex L. Chisholm, Pascale Gaudet, Eric M. Just, Karen E. Pilcher, Petra Fey, Sohel N. Merchant, and Warren A. Kibbe. dictyBase, the model organism database for Dictyostelium discoideum. *Nucleic Acids Research*, 34, 2006.

[5] Albert Goldbeter. Oscillations and Waves of Cyclic AMP in Dictyostelium: A prototype for Spatio-Temporal Organization and Pulsatile Interellular Communication. *Bulletin of Mathematical Biology*, 68, 1095-1109, 2006.

[6] Sarah Annesley and Paul R. Fisher. Dictyostelium discoideum- a model for many reasons. *Mol Cell Biochem*, 329:73-91, 2009.

[7] Kirsten F. Swaney, Chuan-Hsiang Huang, and Peter N. Devreotes. Eukaryotic Chemotaxis: A Network of Signaling Pathways Controls Motility, Directional Sensing, and Polarity . *Annu. Rev. Biophys.*, 39:265-89, 2010.

[8] Atsuo T. Sasaki, Cheryl Chun, Kosuke Takeda, and Richard A.. Firtel. Localized Ras signaling at the leading edge regulates PI3K, cell polarity, and directional cell movement. *The Journal of Cell Biology*, 167, 2004.

[9] Arjan Kortholt, Ineke Keizer-Gunnink, Rama Kataria, and J.M. Van Haastert. Ras activation and symmetry breaking during Dictyostelium Chemotaxis. *Journal of Cell Science*, 126, 4502-4513, 2013.

[10] Arjan Kortholt, Rama Kataria, Ineke Keizer-Gunnink, Wouter N. Van Egmond, Ankita Khanna, and Peter J.M. van Haastert. Dictyostelium chemotaxis: essential Ras activation and accessory signaling pathways for aplification. *European Molecular Biology Organization*, 12, 2011.

[11] Yochiro Kamimura, Huaqing Cai, and Peter N. Devrotes. TORC2 ad Chemotaxis in Dictyostelium discoideum. *The enzymes*, 28, 2010.

[12] Tian Jin. Gradient sensing. *Current opinion in Cell Biology*, 25:532-537, 2013.

[13] Mary Ecke and Günter Gerish. Co-existence of Ras activation in a chemotactic signal transduction pathway and in an autonomous wave - forming system. *Small-GTPases*, 10:1, 72-80, 2017.

[14] Günther Gerisch, Britta Schroth-Diez, Annette Müller-Taubenberger, and Mary Ecke. PIP3 Waves and PTEN Dynamics in the Emergence of Cell Polarity. *Biophysical Journal*, 103:1170-1178, 2012.

[15] Tatsuo Shibata, Masatoshi Nishikawa, Satomi Matsuoka, and Ueda Masahiro. Modeling the self-organized phosphatidylinositol lipid signaling system in chemotactic cells using quantitative image analysis. *Journal of Cell Science*, 125, 5138-5150, 2012.

[16] May Anne Mata, Megha Dutot, Leah Edelstein-Keshet, and William R. Holmes. A model for intracellullar actin waves explored by nonlinear perturbation analysis. *Journal of Theoretical Biology*, 334, 2013.

[17] Mathias Gerhardt, Mary Ecke, Michael Waiz, Andreas Stengi, Carsten Beta, and Günther. Gerisch. Actin and PIP3 waves in giant cells reveal the inherent length scale of an excited state. *Journal of Cell Science*, 127:4507-4517, 2014.

[18] Olivier Hoeller and Robert R. Kay. Chemotaxis in the Absence of PIP3 Gradients. *Current Biology*, 17:813-817, 2007.

[19] Hans Meinhardt. Orientation of chemotactic cells and growth cones: models and mechanisms. *Journal of Cell Science*, 112:2867-2874, 1999.

[20] Sergio Alonso, Maike Stange, and Carsten Beta. Modeling random crawling, membrane deformation and intracellular polarity of motile amoeboid cells. *Plos One*, 13(8), 2018.

[21] Peter J.M. van Haastert, Ineke Keizer-Gunnink, and Arjan Kortholt. Coupled excitable Ras and F-actin activaion mediates spontaneous pseudopod formation and directed cell movement. *Molecular Biology of the Cell*, 28, 2017.

[22] Varunyu Khamviwath, Jifeng Hu, and Hans G. Othmer. A contunuum Model of Actin Waves in Dictyostelium discoideum. *Plos One*, 8, 2013.

[23] Danying Shao, Wouter-Jan Rappel, and Herbert Levine. A computational model for cell morphodynamics. *Phys. Rev. Lett*, 105(10), 2010.

[24] Eduardo Moreno, Sven Flemming, Francesc Font, Matthias Holschenider, Carsten Beta, and Sergio Alonso. Modelling cell crawling strategies with a bistable model: From amoeboid to fan-shaped cell motion. *Physica D*, 412, 2020.

[25] Sven Flemming, Francesc Font, Sergio Alonso, and Carsten Beta. How cortical waves drive fission of motile cells. *PNAS Latest Articles*, 2019.

[26] Markus Lange, Jana Prassler, Mary Ecke, Annette Müller-Taubenberger, and Günther Gerisch. Local Ras activation, PTEN pattern, and global actin flow in the chemotactix responses of oversized cells. *Journal of Cell Science*, 129, 3462-3472, 2016.

[27] Martin Meier-Schellersheim, Xuehua Xu, Bastian Angermann, Eric J. Kunkel, Tian Jin, and Ronald N. Germain. Key Role of Local Regulation in Chemosensing Revealed by a New Molecular Interaction-Based Modeling Method. *PLoS Computational Biology*, 2, 7:82, 2006.

[28] Satoru Funamoto, Ruedi Meili, Susan Lee, Lisa Parry, and Richard A. Firtel. Spatial and Temporal Regulation of 3-Phosphoinositides by PI 3-Kinase and PTEN Mediates Chemotaxis. *Cell*, 109:611-623, 2002.

[29] Boris N. Kholodenko. Cell-signaling dynamics in time and space. *Nature Reviews: Molecular Cell Biology*, 105:7, 2006.

[30] Satomi Matsuoka and Masahiro Ueda. Mutual inhibition between PTEN and PIP3 generates bistability for polarity in motile cells. *Nature communications*, 9:4481, 2018.

[31] Tian Jin, Xuehua Xu, and Dale Hereld. Chemotaxis, chemokine receptors and human disease. *Cytokine*, 44: 1-8, 2008.

[32] Silva T.A., Garlet G.P., Fukada S.Y., Silva J.S., and Cuhna F.Q. Chemokines in Oral Inflammatory Diseases: Aplical Periodontitis and Periodontal Disease. *Critical Reviews in Oral Biology Medicine*, 86(4):306-319, 2007.

Appendices

Table 1: Time and spatial discretization for the simulations

Parameter	Definition	Value
dx	Spatial discretization	0.314 μm
dt	Temporal discretization	0.005 s

Table 2: List of the values of the parameters for Ras simulations from [3]

Parameter	Definition	Value
V_{GAPs}	Deactivation rate of Ras by GAPs	16 s^{-1}
K_{GAPs}	Deactivation reaction Michaelis constant of GAPs	40 $molecules\mu m^{-2}$
V_{GEFs}	Activation rate of Ras by PI3K	$400-600$ s^{-1}
K_{GEFs}	Activation reaction Michaelis constant of GEFs	3500 $molecules\mu m^{-2}$
$V_{feedback}$	Reaction rate of PIP3 feedback regulation	25 s^{-1}
K_{PIP3}	PIP3 feedback regulation Michaelis constant	0.1 $molecules\mu m^{-2}$
$\lambda_{Ras-GTP}$	Ras-GTP dissociation rate	0.2 s^{-1}
$\lambda_{Ras-GDP}$	Ras-GDP dissociation rate	0.003 s^{-1}
k	Ras-GDP association rate	45 $molecules\mu m^{-2}s^{-1}$
$V_{GAPs_{ass}}$	GAPs association rate by Ras-GDP	1300 $molecules\mu M^{-1}\mu m^{-2}s^{-1}$
K_{RasGDP}	Association reaction Michaelis constant of GAPs	3000 $molecules\mu m^{-2}$
λ_{GAPs}	GAPs dissociation rate	1.2 s^{-1}
K_α	Half-maximum [Ras-GTP] for GAPs negative regulation	120 $molecules\mu m^{-2}$
α	Magnitude of GAPs negative regulation	0.001
$GAPs_{total}$	Total GAPs concentration	0.1 μM
$[Ras-GTP]_{initial}$	Ras-GTP initial value	1000 $molecules\mu m^{-2}$
$[Ras-GDP]_{initial}$	Ras-GDP initial value	1000 $molecules\mu m^{-2}$
$[GAPs]_{initial}$	GAPs initial value	0 $molecules\mu m^{-2}$

Table 3: List of the values of the parameters for PIP3 simulations from [3]

Parameter	Definition	Value
V_{PTEN}	Dephosphorylation rate of PIP3 by PTEN	3 s^{-1}
K_{PTEN}	Dephosphorylation reaction Michaelis constant of PTEN	500 μm^{-2}
V_{PI3K}	Phosphorylation rate of PIP2 by PI3K	12 s^{-1}
K_{PTEN}	Phosphorylation reaction Michaelis constant of PI3K	300 μm^{-2}
$V_{PTEN_{ass}}$	PTEN association reaction rate by PIP2	5000 $molecules\mu M^{-1}\mu m^{-2}s^{-1}$
K_{PIP2}	Association reaction Michaelis constant of PTEN	2000 μm^{-2}
λ_{PIP3}	PIP3 degradation rate independent of PTEN	0.2 s^{-1}
β	Magnitude of PI3K activation by Ras-GTP	0.01
χ	Transformation constant from surface to volume concentration	0.001 $molecules\mu M\mu m^{-2}$
$PTEN_{total}$	Total PTEN concentration	0.1 μM
PIP_{total}	Total PIP density on plasma membrane	5000 $molecules\mu m^{-2}$
R	Cell radius	5 μm
D	Molecules Diffusion coefficient on plasma membrane	0.2 $\mu m^{-2}s^{-1}$
$[PIP3]_{initial}$	PIP3 initial value	0 $molecules\mu m^{-2}$
$[PIP2]_{initial}$	PIP2 initial value	5000 $molecules\mu m^{-2}$
$[PTEN]_{initial}$	PTEN initial value	0 $molecules\mu m^{-2}$